FROM RIVERS TO NATURAL GAS: THE INFLUENCE OF ALLOCHTHONOUS INPUTS ON MARINE NITROGEN FIXATION AND THE CARBON CYCLE

A Thesis
Presented to
The Academic Faculty

by

Sarah C. Weber

In Partial Fulfillment
of the Requirements for the Degree
Master of Science in the
School of Biology

Georgia Institute of Technology
December 2015

FROM RIVERS TO NATURAL GAS: THE INFLUENCE OF ALLOCHTHONOUS INPUTS ON MARINE NITROGEN FIXATION AND THE CARBON CYCLE

Approved by:

Dr. Joseph P. Montoya, Advisor
School of Biology
Georgia Institute of Technology

Dr. Samantha B. Joye
Department of Marine Sciences
University of Georgia

Dr. Frank J. Stewart
School of Biology
Georgia Institute of Technology

Date Approved: November 20, 2015

To my family
&
closest friend

ACKNOWLEDGEMENTS

I would like to thank my mother and father, without whom I would quite literally not be here. To my mom for cultivating my interest in science from such a young age and helping me see that teaching isn't all that bad; to my dad, my scientific idol, for showing me the power of eternal optimism; and to Jola, for their support from afar and liquid motivation. Thank you to all the friends I've made along the way – there are too many to name but y'all know who you are. All of you have made my time at Georgia Tech not only bearable, but incredibly rich. Thank you to the members of my committee – Joe Montoya, Mandy Joye, and Frank Stewart – for the guidance along the way and for enabling the next stage of my adventures.

Most of all I would like to thank Joe Montoya, to whom I owe so much. You have trained me to be a scientist, but more importantly, you have made me an oceanographer.

TABLE OF CONTENTS

LIST OF TABLES

LIST OF FIGURES

SUMMARY

The Western Tropical North Atlantic (WTNA) was once thought to be a net source of carbon dioxide (CO_2) to the atmosphere, but recent studies have shown that this Amazon River influenced region may actually act as a net sink for CO_2. During a 2010 research cruise to the WTNA, we characterized the impact of the Amazon River on offshore diazotrophy (N_2-fixation) and the resulting stimulation of biological carbon export from surface waters. Through the delivery of phosphate- and silicate-replete waters to the nitrogen (N) limited surface waters of the WTNA, the aging Amazon River plume promotes the growth of diatom-diazotoph associations (DDAs). Regions supporting large DDA blooms were associated with increased pCO_2 and DIC drawdown in the surface waters, reflecting the net export of carbon from the mixed layer.

The existence of this biologically mediated linkage between the C and N cycles in productive surface waters is well known, but we have only recently discovered a stimulatory relationship in deep waters between oil/gas release and N_2-fixation. This association was first observed after the Deepwater Horizon oil spill in 2010 and we again saw evidence for it in the days following the Hercules 265 natural gas blowout. This blowout event was characterized by the release of an unknown quantity of natural gas into the shelf waters of the Northern Gulf of Mexico, but we detected a response from the marine microbial community within days. We observed a significant drawdown of dissolved oxygen and found

biogeochemical evidence for the incorporation of methane-carbon into the food web, along with a modest stimulation of N_2-fixation.

The episodic nature of anthropogenic blowouts makes them difficult to study, so we use cold seeps in the Gulf of Mexico as natural analogues. Interestingly, we have measured both methane oxidation and N_2-fixation at depth above some of the more active seeps. Using NanoSIMS analyses, we have taken the first steps towards physically characterizing the organisms utilizing these metabolisms. It appears that different organisms are carrying out these processes, with CH_4-assimilation occurring primarily in individual particles or small aggregates, whereas N_2-fixtion was associated with larger, sulfur-containing aggregates. Continued NanoSIMS work in combination with the use of microbial ID techniques will help to further characterize these unique deepwater diazotrophs.

CHAPTER 1

INTRODUCTION

Nitrogen (N) availability limits primary production in much of the world's oceans, particularly in oligotrophic gyres (Smith 1984; Codispoti 1989; Zehr & Ward 2002). Some organisms, called diazotrophs, can metabolically overcome this limitation by converting nitrogen gas (N_2) into biologically available N through N_2-fixation. This process, which provides a "new" source of N to the pool of biologically available N (Dugdale & Goering 1967), supports considerable biomass in the surface oceans (Capone et al. 1997; Montoya et al. 2004). In terms of the global N budget, N_2-fixation is opposed by dentrification, a process in which N is removed from this reactive pool as N_2. The balance between supply and demand in the oceanic pool of nitrogen remains unresolved, as estimates of dentrification have continued to rise (Codispoti et al. 2001). Regardless of whether the N cycle is currently at steady state, marine N_2-fixation plays a very important role in sustaining primary production in the world's oceans.

As a driver of new production, N_2-fixation also has important effects on the global C cycle, predominantly through the biological carbon pump, which drives the downward movement of carbon from the atmospheric pool of CO_2 to the deep ocean (Eppley & Peterson 1979; Gruber & Sarmiento 2002). As primary producers fix carbon, they remove CO_2 from surface waters. When these phytoplankton senesce or are consumed by zooplankton and packaged into fecal pellets, some of this organic matter escapes recycling in the surface waters and sinks to depth, promoting a net export of carbon from the mixed layer. The strength of the biological pump, or the magnitude of export

production, depends on the concentrations and sources of nutrients in the surface waters (Gruber & Sarmiento 2002). In this context, large rivers (e.g. the Amazon, Congo, and Mekong Rivers) that inject substantial quantities of water and nutrients into the ocean are capable of enhancing vertical carbon export far offshore.

Conventionally, large rivers have been considered net sources of CO_2 because of significant degassing during mixing of riverine with oceanic waters (Takahashi et al. 2002; Mikaloff Fletcher et al. 2007). Similarly, the primary impact of rivers on carbon export has been thought to be limited to coastal waters, where riverine nutrients support classical eutrophication (Eppley & Peterson 1979; Longhurst 1993; Lohrenz et al. 1997). Since most of the ocean is N limited, river-derived N is consumed very quickly as the fresh water mixes with the coastal ocean, whereas phosphorous (P) and silicate (Si) are often transported much farther offshore in the river plume. These aging plume conditions produce strong nitrogen limitation, which favors the growth of diazotrophs, including diatom-diazotroph associations (DDAs; Foster et al. 2007; Subramaniam et al. 2008). Recent work has shown that these DDAs, which are ballasted by the silica frustules of the diatoms, contribute substantially to export production in the outer reaches of large river plumes (Voss et al. 2006; Subramaniam et al. 2008; Foster et al. 2009). The large export flux driven by DDAs can ultimately make these systems net sinks of CO_2 (Subramaniam et al. 2008).

The linkage between nitrogen fixation in surface waters and the biological carbon pump has been well characterized, but we have only recently found evidence for a poorly recognized relationship between deep-water nitrogen fixation and anthropogenic/natural releases of natural gas. The Gulf of Mexico supports diverse pelagic ecosystems,

including large surface blooms of diazotrophic *Trichodesmium* spp., all of which flourish in the presence of thousands of active cold seeps releasing oil and gas into the water column. The massive reservoirs of petro-carbon beneath the GoM seafloor have long attracted the attention of petroleum companies, though sometimes with disastrous effects.

The Deepwater Horizon oil spill of 2010 marked the largest such disaster in history, with the release of an estimated 5 million barrels of oil and over 350,000 tonnes of methane and other gases (Joye et al. 2011). Though large quantities of oil and gas made it to the surface, a large plume of oil and gas at ~1000 m depth moved laterally to the southwest of the wellhead (Camilli et al. 2010; Valentine et al. 2010). During a research cruise 1 month after the well was sealed, we measured both low $\delta^{13}C$ and low $\delta^{15}N$ in suspended particles within this deep plume (Fernández et al., in review). The low $\delta^{13}C$ signatures are attributable to incorporation of ^{13}C-depleted petro-carbon into particulate organic matter, but this process alone would not affect the nitrogen isotopic composition of particulate matter. Low $\delta^{15}N$ signatures (-2 to 0 ‰, Montoya et al. 2007), are typically associated with nitrogen fixation. In addition to ^{15}N depletion in particles within the deep-water plume, we also measured significant rates of N_2-fixation within the plume layer using the stable isotope tracer method (Montoya et al., in prep). This was a surprising finding, given the high ambient concentrations of nitrate, which can be used by many organisms as a substrate for growth. This represents a previously undescribed linkage between the C and N cycles deep in the water column.

During cruises the following summer, we found that the biogeochemical influence of the deep subsurface plume, as well as its direct imprint, were greatly reduced. Though our cruises could broadly define the duration of the impact of this DWH oil spill feature,

much remains to be known about the timescale of influence of such events. In the summer of 2013, we were fortunate to study a natural gas blowout just days after it began, when a rig off the coast of Louisiana lost control of one of its wells. Interestingly, we documented a biogeochemical response similar to that of the DWH deep plume, though on much shorter spatial and temporal scales (Weber et al., in press). We saw clear evidence for the incorporation of methane-derived C into particles with a modest stimulation of N_2-fixation.

As a natural analogue to anthropogenic releases of oil/gas, we have studied the influence of cold seeps on local N and C cycling in the water column. Using combined $^{15}N_2$ and $^{13}CH_4$ tracer additions in paired "in plume" and "out of plume" experiments, we have found replicated evidence for the stimulation of N_2-fixation in the water column above active seeps, though we have not yet been able to quantify the assimilation of CH_4 into bulk biomass (Montoya et al., in prep).

In an effort to better characterize the relationship between CH_4 oxidizers and diazotrophs, we took advantage of NanoSIMS (nano-scale Secondary Ion Mass Spectrometry) technology, which can provide spatially resolved isotope measurements on a sub-micrometer scale (summarized by Hoppe et al. 2013). The secondary ion mass spectrometry (SIMS) analytical technique considered here uses a cesium (Cs^+) ion microprobe to ablate a small section of a sample, a process called sputtering. A fraction of the sputtered atoms are ionized (secondary ions) and accelerated towards the mass spectrometer, where they are separated based on their charge to mass ratio. These secondary ions (in this case $^{12}C^-$, $^{13}C^-$, $^{16}O^-$, $^{12}C^{14}N^-$, $^{12}C^{15}N^-$, and $^{32}S^-$) are measured simultaneously with the use of multiple electron multiplier detectors. By moving the Cs^+

ion probe over the sample in a raster pattern, an ion image of high-spatial resolution can be formed, allowing for the visualization of stable isotope distributions in a sample. Ultimately, this approach can provide unparalleled insight into the size, shape, and distribution of the organism(s) stimulated to oxidize methane and fix nitrogen near anthropogenic and natural releases of oil and gas.

CHAPTER 2

AMAZON RIVER INFLUENCE ON NITROGEN FIXATION AND CARBON EXPORT IN THE WESTERN TROPICAL NORTH ATLANTIC[†]

Sarah C. Weber[1], Edward J. Carpenter[2], Victoria J. Coles[3], Patricia L. Yager[4], Joaquim Goes[5], and Joseph P. Montoya[1]

[1] School of Biology, Georgia Institute of Technology, 311 Ferst Drive, Atlanta, GA, 30332, USA

[2] Romberg Tiburon Center, San Francisco State University, Tiburon, CA 94920 USA

[3] University of Maryland Center for Environmental Science, Horn Point Laboratory, Cambridge, MD 21613 USA

[4] School of Marine Programs, University of Georgia, Athens, GA 30602 USA

[5] Lamont-Doherty Earth Observatory, Columbia University, Palisades, NY 10964 USA

[†] Manuscript in preparation; an early version of this chapter was part of SCW's undergraduate research thesis.

2.1 Abstract

As part of the ANACONDAS program, we characterized the distribution of nutrients, particulate organic matter, phytoplankton, and stable carbon and nitrogen isotopes in the Amazon plume during high-discharge (May-June 2010). We encountered low salinity (16.6) to the south, where the plume was most spatially coherent, and high salinity (36.0) to the east. The major nutrients varied distinctly with salinity, with NO_3^- + NO_2^- largely absent from the plume and SiO_2 and PO_4^{3-} showing different degrees of conservative behavior. SiO_2 behaved more conservatively, with negative deviations reflecting biological consumption, whereas PO_4^{3-} showed positive deviations across a broad range of salinities. These distributions resulted in strong N limitation and delivery of SiO_2 and PO_4^{3-} offshore creating conditions that favored diazotrophy. We found a variety of diazotrophs in our study area, with interesting contrasts in their distributions. Mesohaline waters to the northwest of the plume were dominated by Diatom-Diazotroph Associations (DDAs), particularly *Hemiaulus hauckii – Richelia intracellularis*. In contrast, *Trichodesmium* spp. were most abundant in the southeast. These diazotrophs impacted the nitrogen and carbon budgets in fundamentally different ways, with *H. hauckii* making much greater contributions to the particulate nitrogen pool and to CO_2 drawdown than *Trichodesmium* spp., leading to much higher export fluxes. Our findings provide an important constraint on the role of the Amazon plume in creating distinct niches and roles for diazotrophs in the nutrient and carbon budgets of the Western Tropical North Atlantic.

2.2 Introduction

The Amazon River contributes nearly one fifth of the global riverine freshwater input to the ocean and is fed by the largest drainage basin in the world, encompassing nearly 6 million km^2 of land (Vorosmarty et al. 2000). The tremendous volume of water discharging from the Amazon forms a very dynamic and extensive surface plume that protruded well offshore into the Western Tropical North Atlantic (WTNA). During the spring and summer months, the plume follows the North Brazil Current (NBC) along the northeastern coast of South America, carrying low salinity water to the Caribbean. In the fall and winter, the plume retroflects to the east as it becomes entrained in the North Equatorial Countercurrent (NECC; Muller-Karger et al. 1988; Lentz & Limeburner 1995; Fratantoni & Glickson 2002). Early studies suggested that the primary impact of the Amazon River plume on phytoplankton growth was constrained to coastal waters near the river mouth, whereas the large blooms in the retroflection were supported predominantly by local upwelling of nutrients (Longhurst 1993). More recent fieldwork has begun to reveal the full extent of the river's influence on the ecology and biogeochemistry of the WTNA, including direct stimulation of primary production and diazotrophy (biological N_2-fixation) hundreds of kilometers from the coast (Muller-Karger et al. 1995; Subramaniam et al. 2008).

The tropical North Atlantic was formerly considered a net source of CO_2 (~30 TgC y^{-1}; Takahashi et al. 2002; Mikaloff Fletcher et al. 2007) to the atmosphere, but new estimates of production supported by riverine nutrient inputs and diazotrophy suggest that the western side of the basin may act as a net sink, sequestering ~28 TgC y^{-1} (Kortzinger 2003; Subramaniam et al. 2008). New nitrogen from diatom-diazotroph associations

(DDAs) and free-living N_2-fixers common in oligotrophic waters (e.g. *Trichodesmium* spp.) supports high rates of primary production throughout the plume region (Carpenter et al. 2004; Foster et al. 2007; Subramaniam et al. 2008). DDAs are hypothesized to play an especially important role in ocean-atmosphere carbon exchange; as DDA blooms senesce or are consumed and defecated by zooplankton, their high silica content promotes rapid sinking through the water column. This process, referred to as the biological pump, results in the drawdown of atmospheric CO_2 and ultimately the sequestration of carbon in deep ocean sediments (Eppley & Peterson 1979; Gruber & Sarmiento 2002).

In order to better understand the mechanisms that drive biologically mediated carbon export in the WTNA, we embarked on a research cruise to the Amazon plume in spring 2010 as part of the multidisciplinary ANACONDAS program (Amazon iNfluence on the Atlantic: CarbOn export from Nitrogen fixed by DiAtom Symbioses). We used shipboard underway sampling and CTD-rosette systems to characterize over 450,000 km^2 of surface waters, generating high-resolution maps of nutrient concentrations, phytoplankton, and stable isotope natural abundances. With these data we have better identified the plume conditions that impact diazotroph distributions and their contribution to the N and C budgets of the WTNA.

2.3 Methods & Materials

2.3.1 Hydrographic Properties

Seawater and particle samples were collected on R/V *Knorr* cruise KN197-8 (May 22, 2010 – June 24, 2010) to the Amazon Plume region (Fig. 2.1 A). Here, we focus on surface processes and have included only surface layer samples from CTD-rosette casts in our analyses. In addition to our hydrocasts, we used the shipboard underway seawater system (intake at ~4.5 m; lines were bleached and well flushed prior to the cruise) to characterize hydrographic properties. In regions where plume thickness was close to the ship's intake depth, measurements from nearby CTD casts were compared to those from underway samples and were found to be in agreement. Discrete underway samples were collected at roughly hourly intervals while steaming between stations beginning with station 9 (3 June 2010) and continuing through the remainder of the cruise. Due to the delayed start of underway sample collection along our cruise track, none of our underway samples were obtained in fully oceanic waters, whereas surface CTD-rosette samples included the full salinity range we encountered on this cruise.

Seawater samples for nutrient analysis were collected directly (unfiltered) from the ship's seawater system or from the CTD-rosette. All of our nutrient samples (NO_3^- + NO_2^-, PO_4^{3-}, SiO_2) were analyzed at sea using a Lachat QuickChem 8000 FIA system. We assessed the impact of conservative mixing of plume and offshore waters on nutrient distributions by performing a linear regression between averaged nutrient concentrations from waters with the lowest measured salinities (avg 17.95, n = 6) and from offshore oceanic stations (avg 35.62, n = 6) southeast of the plume (Table 2.1).

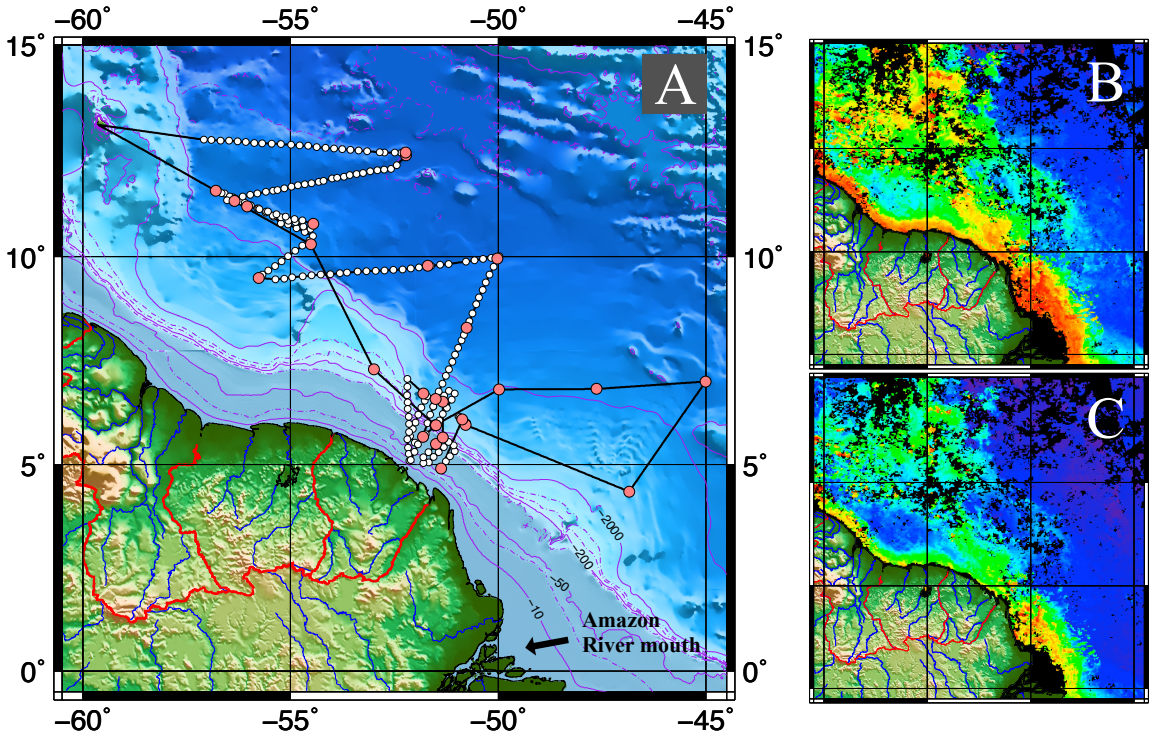

Figure 2.1: (**A**) Cruise track of R/V Knorr cruise KN197-8 in spring 2010 off the northeastern coast of South America. (**B**) Composite of MODIS-Aqua chlorophyll *a* images for the period of the cruise. (**C**) Composite of kd490 satellite images for the period of the cruise.

End-Member	Salinity (psu)	PO_4^{3-} (µM)	SiO_2 (µM)
River	17.95 ± 0.61	0.53 ± 0.04	50.0 ± 3.39
Oceanic	35.62 ± 0.24	0.03 ± 0.04	1.13 ± 0.73

Table 2.1: End-member salinity and nutrient concentrations (mean ± SE) used to calculate conservative mixing relationships. River and oceanic end-member values (n = 6 each) were from samples at the lowest measured salinity and from oceanic stations to the SE, outside of the plume influence.

Suspended particles (e.g., phytoplankton, detritus) were collected by gentle pressure filtration (5-10 psi) of 2-18 L of seawater through pre-combusted (450° C for 2 h) 47-mm GF/F filters that were then dried at 60° C and stored over desiccant for analysis ashore.

Measurements of surface pCO_2 were made using an underway pCO_2 system (Sweeney et al. 2000) with a showerhead equilibrator and a non-dispersive infrared CO_2 gas analyzer (LICOR 6252), and were standardized using five CO_2-air reference gas mixtures from NOAA's Climate Monitoring and Diagnostics Laboratory. The precision of our pCO_2 measurements was ± 1 µatm. ΔpCO_2 (observed – atmosphere) was scaled to estimated plume thickness (scaled ΔpCO_2) by multiplying ΔpCO_2 by a plume thickness factor (*ptf*), allowing us to relate underway measurements to profile data obtained at hydrographic stations. We defined *ptf* from the relationship between plume thickness and salinity at our hydrographic stations (not shown), and UW samples were binned according to the following criteria: $S < 25$, $ptf = 1$; $25 \leq S < 30$, $ptf = 1.5$; $30 \leq S < 35$, $ptf = 3$; $S \geq 35$, $ptf = 5$.

Surface DIC samples were taken from the CTD-rosette according to standard protocols (Dickson et al. 2007). Concentrations were measured on preserved samples using standard protocols (Cooley & Yager 2006) at the University of Georgia with a SOMMA/coulometer (Johnson et al. 1993; 1998) with ~0.5 µmol kg^{-1} precision. DIC measurements were checked for accuracy using Certified Reference Materials. Biological depletion of DIC (ΔDIC_{bio}) was calculated using methods from Cooley & Yager (2006). We used trapezoidal integration of multiple CTD-rosette samples located

within the plume to estimate the areal impact of biological uptake of DIC (integrated ΔDIC_{bio}).

2.3.2 Phytoplankton Communities

Samples for phytoplankton enumeration were collected by gently filtering 2 - 4 L of seawater from the flow-through system or the CTD-rosette through 20 μm Nitex mesh. The samples were gently backwashed off the mesh with about 50 mL of filtered seawater and then fixed with acidic Lugol's solution. A well-mixed 15 mL aliquot from this tube was then centrifuged at 2000 rpm for 20 minutes and 14 mL of supernatant was drawn off. The cells within the remaining 1 mL were resuspended and placed in a Sedgwick-Rafter counting chamber for enumeration. Transects were then counted at 320X using a long working distance objective on a Zeiss Axioskop microscope.

An Advanced Laser Fluorometer (ALF), which is capable of distinguishing multiple phytoplankton pigments, was connected to the ship's seawater flow-through system on all transits between stations. Using the ALF in conjunction with other instruments allowed for continuous measurements of salinity, temperature, and fluorometric Chl *a* in water from approximately 4.5 m below the surface along the cruise track shown in Fig. 2.1. With the exception of a few breaks for reconditioning, the ALF was operated throughout the cruise, providing essentially real time distribution patterns of hydrographic, chemical, and biological properties over a distance of 700 km inside and outside the plume.

2.3.3 Elemental & Isotopic Analyses

All elemental concentration and stable isotope natural abundance measurements were made by continuous-flow isotope-ratio mass spectrometry (CF-IRMS) using a

Micromass Optima interfaced to a Carlo Erba NA2500 elemental analyzer. All stable isotope abundances are reported as $\delta^{15}N$ and $\delta^{13}C$ values relative to atmospheric N_2 and VPDB, respectively. Each analytical run included a size series of elemental (methionine) and isotopic (peptone) standards, which provided a check on the stability of the instrument and allowed us to remove the contribution of any analytical blank from our isotopic measurements (Montoya 2008). We conservatively estimate that the overall analytical precision of our isotopic measurements is better than ± 0.1‰.

2.3.4 Isotope Mixing Model

Diazotroph nitrogen (N_{diazo}) contribution to suspended particles was calculated using the nitrogen isotope mass balance approach (Montoya et al. 2002). Particles at the southern end of our survey area had a $\delta^{15}N$ of about 5‰ (Loick-Wilde et al. 2015), likely reflecting a combination of N derived from the Amazon River and NO_3^- upwelled from deep water – similar to the $\delta^{15}N$ of Atlantic deep-water $\delta^{15}N$ nitrate (4.5‰; Sigman et al. 2000) – simplifying the isotopic systematics. The other major N source for the surface waters of the plume is N_2-fixation, which contributes N with a $\delta^{15}N$ of -2‰ (Montoya et al. 2002). We used the strong isotopic contrast between these two sources of N (nitrate + organic N vs diazotroph N) to estimate % N_{diazo} using a simple linear mixing model:

$$\%\ \mathrm{N}_{diazo} = 100 \cdot \left(\frac{\delta^{15}\mathrm{N}_{particles} - \delta^{15}\mathrm{N}_{(nitrate\ +\ organic\ N)}}{\delta^{15}\mathrm{N}_{diazo} - \delta^{15}\mathrm{N}_{(nitrate\ +\ organic\ N)}} \right) \qquad [2.1]$$

where $\delta^{15}N_{(nitrate + organic\ N)}$ = 5‰ and $\delta^{15}N_{diazo}$ = -2‰.

2.4 Results

2.4.1 Hydrographic Properties

Surface waters (0-5m) ranged in salinity between 16.6 and 36.0 (Fig. 2.2 A, C) and in temperature between 28 and 30.5˚C (not shown). Higher temperatures corresponded with fresher water due to the trapping of solar radiation from the freshwater barrier layer effect (Ffield 2007; Foltz & McPhaden 2009). We defined plume regions based on salinity following the convention of Subramaniam et al. (2008): "low salinity" waters with S < 30; "mesohaline" waters with S = 30-35; and "oceanic" waters with S > 35. Salinity tended to increase northward along the plume axis, but with appreciable local variability within this general trend (Fig. 2.2 A, C).

Plume thickness and width generally increased with distance north along the plume axis, reflecting increased mixing with oceanic water and physical dispersion, consistent with prior observations (Lentz & Limeburner 1995). Plume thickness remained fairly constant in the low salinity plume core, ranging between 4 – 6 m (data not shown). Elsewhere, plume thickness at a given location could vary substantially on a time scale of a few hours, with the most dramatic changes taking place near the plume edges.

The dynamic nature of the plume on longer time scales is also evident in comparisons of salinity and chlorophyll *a* in areas that were sampled on both Legs 1 and 2 (Fig. 2.2 : A vs C, B vs D). Samples were collected ~16 days apart in the southern reaches of the survey area, whereas sampling in the north was separated by ~20 days. Over this time period, it appears that the plume migrated to the west, bringing along with it higher chl *a* concentrations.

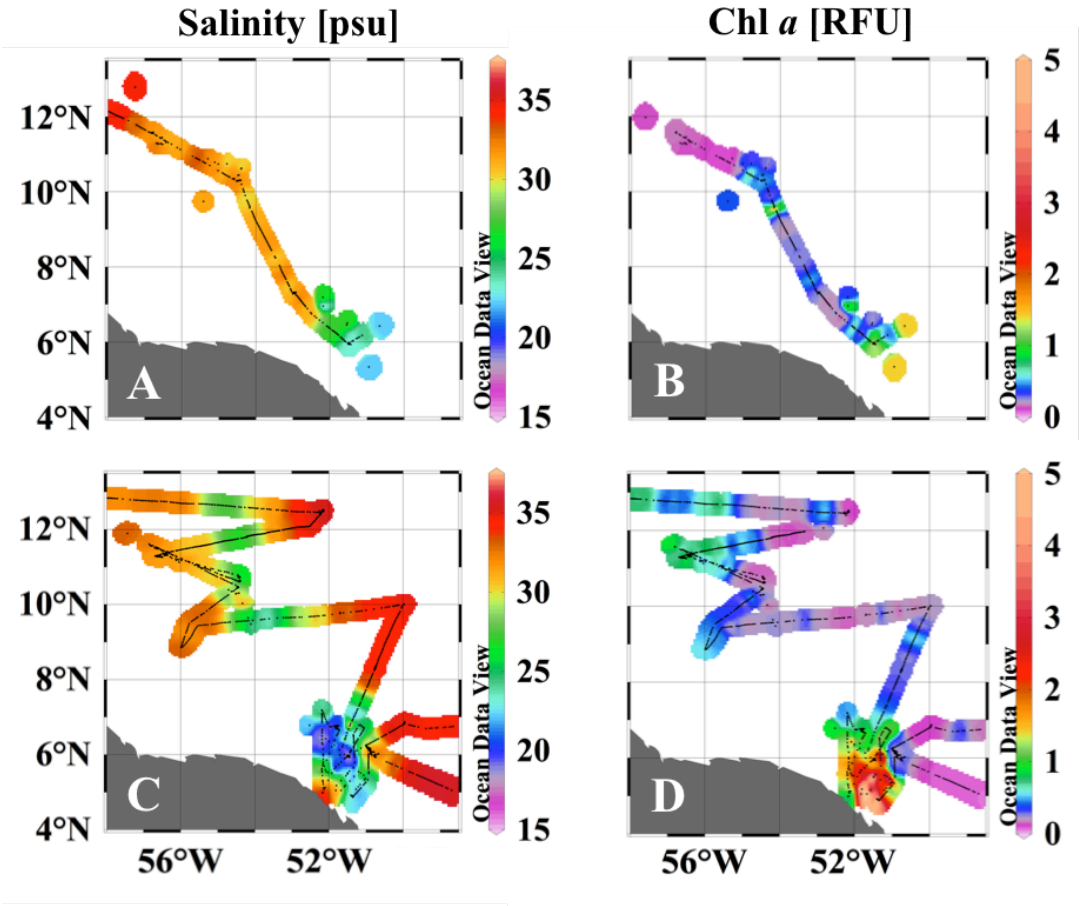

Figure 2.2: Surface distributions of salinity (**A**, **C**) and chlorophyll *a* (**B**, **D**) from Legs 1 (**A**, **B**) and 2 (**C**, **D**) of cruise KN197-8.

2.4.2 Nutrient Distributions

Nitrate + nitrite was mostly absent from surface waters, with only occasionally measurable concentrations distributed across the three salinity regions (Fig. 2.3 A). The maximal value of 0.60 μmol L^{-1} (μM) was located in low salinity plume waters (18.4) at 6˚N 51.5˚W (Fig. 2.4 A).

Phosphate concentrations generally decreased with increasing salinity ($r = -0.342$, $p \leq 0.0001$), ranging from 0.03 to 0.55 μM along the conservative mixing line, but with very strong asymmetrical positive deviations in all salinity regions (Figs. 2.3 B, 2.4 B). These deviations were most pronounced in low salinity waters, where the magnitude of the deviations increased with distance along the plume axis (Fig. 2.4 E).

Silicate concentrations ranged from 0.37 to 49.80 μM and showed generally conservative behavior as a function of salinity ($r = -0.958$, $p \leq 0.0001$; Figs. 2.3 C, 2.4 C), though many stations exhibited departures from the conservative mixing line in the low salinity and mesohaline regions (Fig. 2.4 F). These anomalies were almost exclusively negative, reflecting a deficit of SiO_2 relative to conservative mixing.

2.4.3 Elemental & Isotopic Distributions

Particulate carbon and nitrogen (PC and PN) concentrations showed similar spatial patterns, with the highest concentrations (126.9 μM C, 10.5 μM N) at the southernmost part of the sampled plume (Figs. 2.5 A, B). These elevated values did not coincide with the lowest salinity waters due to the local salinity variation mentioned above. The C and N concentrations dropped sharply at 5.5˚N to ~19 and ~2 μM, respectively, and remained at or slightly below these levels in the northern plume, with the exception of a few elevated measurements to the NW.

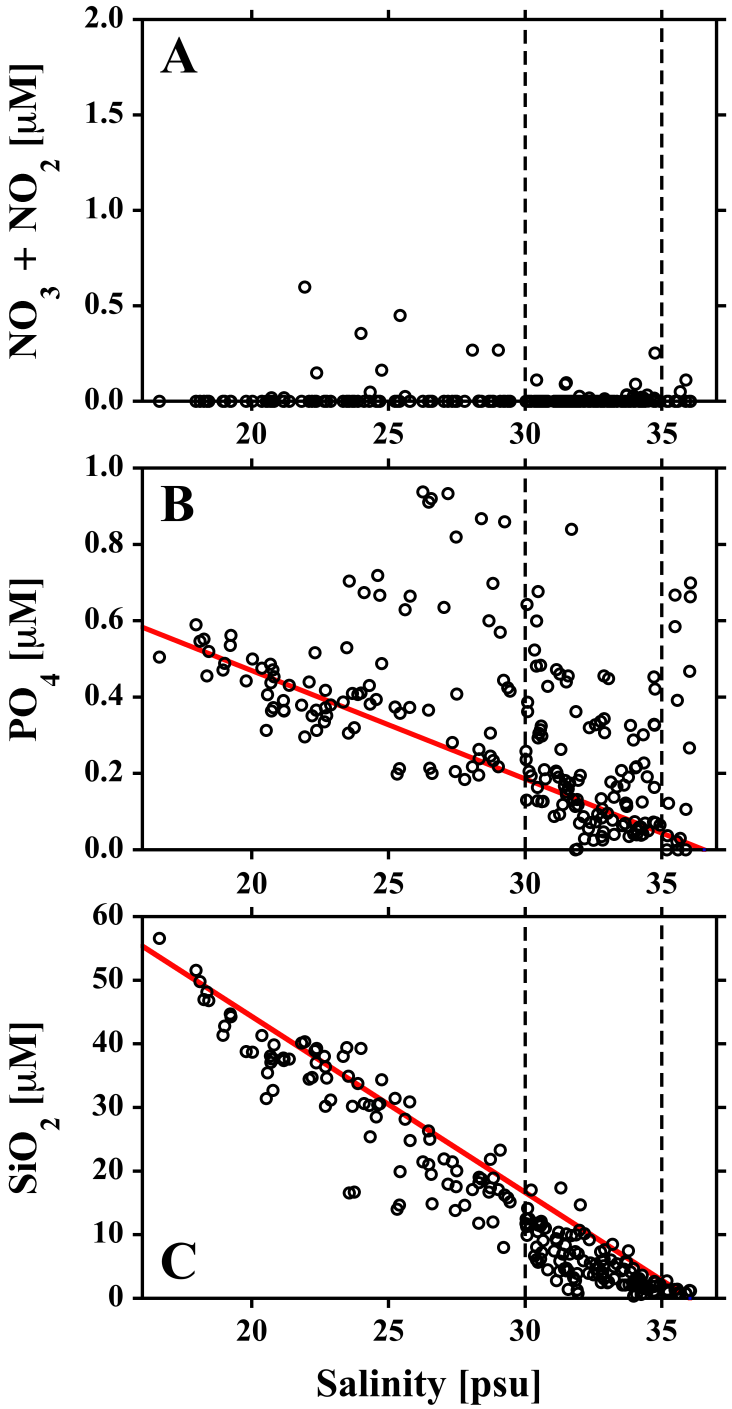

Figure 2.3: Concentrations of NO_3^- + NO_2^- (**A**), PO_4^{3-} (**B**), and SiO_2 (**C**) as a function of salinity. Red lines in (**B**) and (**C**) reflect conservative mixing of plume and oceanic end members and were calculated using nutrient concentrations from the lowest measured salinity (16.6) and from offshore oceanic stations (35.6) SE of the plume. Vertical dashed lines separate the low salinity, mesohaline, and oceanic salinity regions.

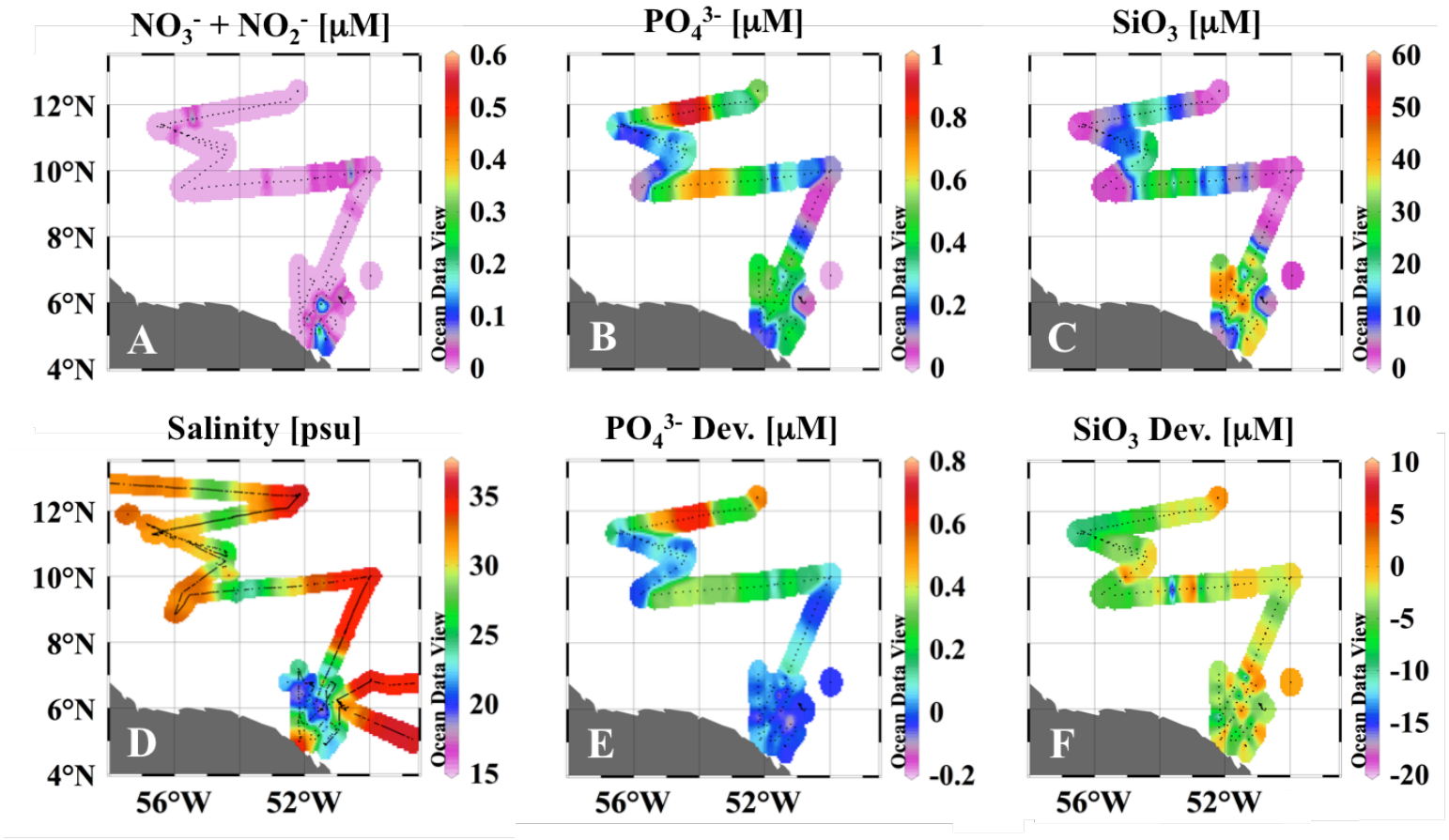

Figure 2.4: Surface distributions of $NO_3^- + NO_2^-$ (**A**), PO_4^{3-} (**B**), and SiO_2 (**C**), salinity (**D**). Panels (**E**) and (**F**) show deviations from conservative mixing of PO_4^{3-} and SiO_2, respectively

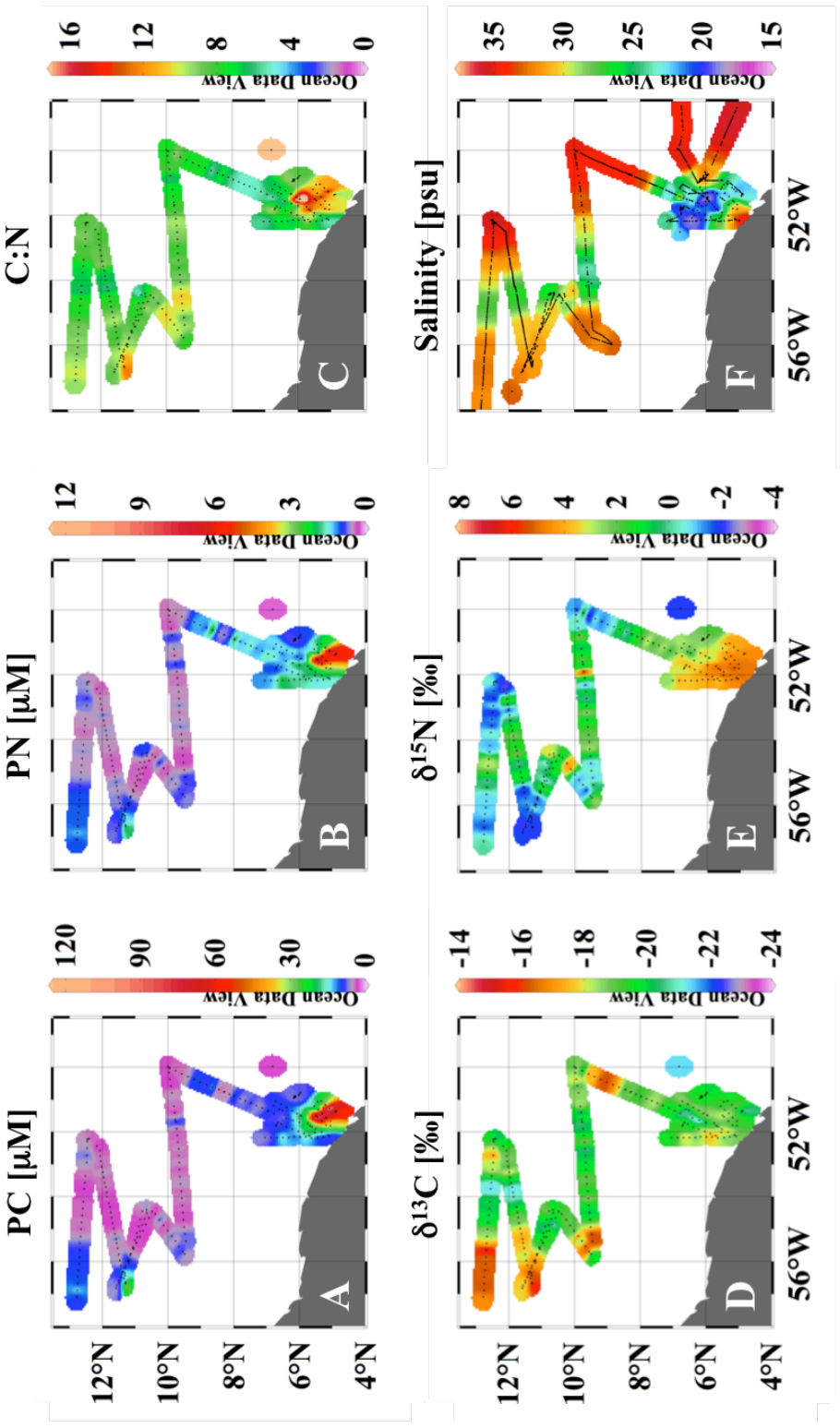

Figure 2.5: Surface distributions of particulate carbon (**A**) and nitrogen (**B**) concentrations, C:N ratios (**C**), and $\delta^{13}C$ (**D**) and $\delta^{15}N$ (**E**) of particles. Panel (**F**) is shows the diazotrophic contribution to particles, % N_{diazo}.

C:N ratios did not follow a monotonic relationship relative to salinity (Fig. 2.5 C). The ratios were highest in the near-shore, low salinity plume (salinity = 9 – 16) and in the mesohaline waters (salinity = 9 – 11) west of the northern plume. There were also two prominent areas along our cruise track characterized by low C:N ratios of 4.5 – 6.6, (below Redfield), extending from the southern plume core between 7 – 9˚N between 11.5 – 12.5˚N in northern plume core.

The $\delta^{13}C$ of suspended particles ranged from -23.7 to -14.6‰ (Fig. 2.6 A). Variation in $\delta^{13}C$ was greater, though positively skewed, in the mesohaline region of the plume, due to a very strong western bias toward much heavier $\delta^{13}C$ (Fig. 2.5 F). Only two small patches of comparably high values were present east of the plume.

The $\delta^{15}N$ of particles ranged between -4.6 and 6.4‰ (Fig. 2.6 B) and showed a general decrease with increasing salinity, except in 17 – 21 salinity waters between 6 – 7˚N (Fig. 2.5 E), where $\delta^{15}N$ increased from 1.9 to 4.5‰. $\delta^{15}N$ was highest in the southern low salinity plume and became more variable with increasing salinity, but tended to decrease in the mesohaline region, approaching low values typical of diazotrophic biomass (ca. -2‰; Montoya et al. 2002). Spatially, these low $\delta^{15}N$ values were located at both the eastern and western edges of the northern plume, with the most negative feature overlapping with the high C and N waters at about 11.5˚N, 56˚W.

2.4.4 Phytoplankton Distributions

Chlorophyll *a* concentrations were highest (6.0 – 11.0 RFU) in the southernmost plume core between 5 – 5.5˚N and decreased to 1.0 RFU to the north up to 6.5˚N (Fig. 2.2 B, D). There was more chl *a* in the western mesohaline waters (0.5 – 0.8 RFU)

compared to the east and everywhere else, where concentrations ranged from the limit of detection to 0.3 RFU.

Trichodesmium spp. and DDAs, primarily *Hemiaulus hauckii* and *Rhizosolenia clevei*, were most abundant in mesohaline waters of the outer plume regions. *H. hauckii* was the dominant diazotroph host, with the highest cell count exceeding 9.7×10^5 cells L^{-1} (Figs. 2.6 C, 2.7 A). The majority of *H. hauckii* biomass was to the west of the plume, though two smaller blooms were present to the east. This spatial distribution of *H. hauckii* correlated very closely with elevated $\delta^{13}C$ ($r = 0.4$; Figs. 2.5 D, 2.7 A). *H. hauckii* was also present in significant concentrations ($5.7\times10^3 – 2.6\times10^4$ cells L^{-1}) in the northern low salinity plume between 10 and 12˚N, but not below this latitude.

R. clevei were far less abundant, with maximum concentrations barely surpassing 800 cells L^{-1} (Figs. 2.6 C, 2.7 C). *R. clevei* was mostly confined to the northernmost mesohaline waters above 11˚N and was slightly more abundant on the eastern side of the plume.

Trichodesmium spp. were broadly distributed and present in significant abundance, but at concentrations much lower than *H. hauckii.* Trichome counts reached 2.0×10^3 trichomes L^{-1}, with a maximum of 3.6×10^3 trichomes L^{-1} east of the southern plume (Figs. 2.6 C, 2.7 B). In general terms, *Trichodesmium* spp. abundance increased on the plume periphery from north to south, with higher concentrations east of the plume, where as *H. hauckii* was more prolific to the west.

2.4.5 Sources of Nitrogen

We used a linear isotopic mixing model (Eqn. 2.1) to calculate the relative contributions of riverine and subsurface $NO_3^- + NO_2^-$ and N_2-fixation to the particulate

nitrogen pool (Montoya et al. 2002). We found that the diazotrophic contribution to nitrogen (% N_{diazo}) increased in magnitude and variability with increasing salinity, with extensive areas of 100% N_{diazo} in the mesohaline and oceanic regions of our cruise track (Fig. 2.7 D). The diazotrophic contribution to particles correlated closely with *H. hauckii* abundance (Figs. 2.7 A, D, and 2.8 A), and was generally ≥ 80% N_{diazo} at all *H. hauckii* bloom locations. N_{diazo} was at or near 100% where both *H. hauckii* and *Trichodesmium* spp. were present in high abundances. At the largest *Trichodesmium* spp. bloom near 6°N, the diazotrophic contribution was only ~50% N_{diazo}, similar to what we observed in surrounding waters (Fig. 2.7 B, D, and 2.8 B).

2.4.6 DIC & pCO_2

Surface pCO_2 concentrations showed a significant correlation (r = 0.84; n = 2908) with salinity, ranging from 100 µatm in low salinity waters to ~400 µatm in oceanic regions (not shown). Variation of up to ± 100 µatm from the trendline reflects variability in the extent of autotrophy versus heterotrophy in the plume (Cooley & Yager 2006). For example, the nearshore area west of the southern plume core exhibited much higher pCO_2 (420 – 480 µatm) at the surface relative to the mesohaline waters to the north (290 – 400 µatm), likely from greater respiration. Depletion relative to atmosphere (ΔpCO_2) was thus most prominent in the low salinity southern plume core, ranging between -220 and -300 µatm. Offshore surface plume thickness varied by 4- to 6-fold, however, so in order to better assess the overall drawdown of CO_2 in the surface layer, we scaled ΔpCO_2 by plume thickness (scaled ΔpCO_2). Integrating through the plume layer revealed that the magnitude of pCO_2 depletion in northern mesohaline waters was actually comparable to that in the southern plume core (Fig. 2.7 E). Plume thickness scaling was also applied

to biological drawdown of DIC (integrated ΔDIC_{bio}) in surface samples, producing similar results (Fig. 2.7 F). Surface drawdown was highest at low salinity stations compared to mesohaline stations and oceanic stations, but when integrated through the mixed layer depth, the impact was largest at the mesohaline stations.

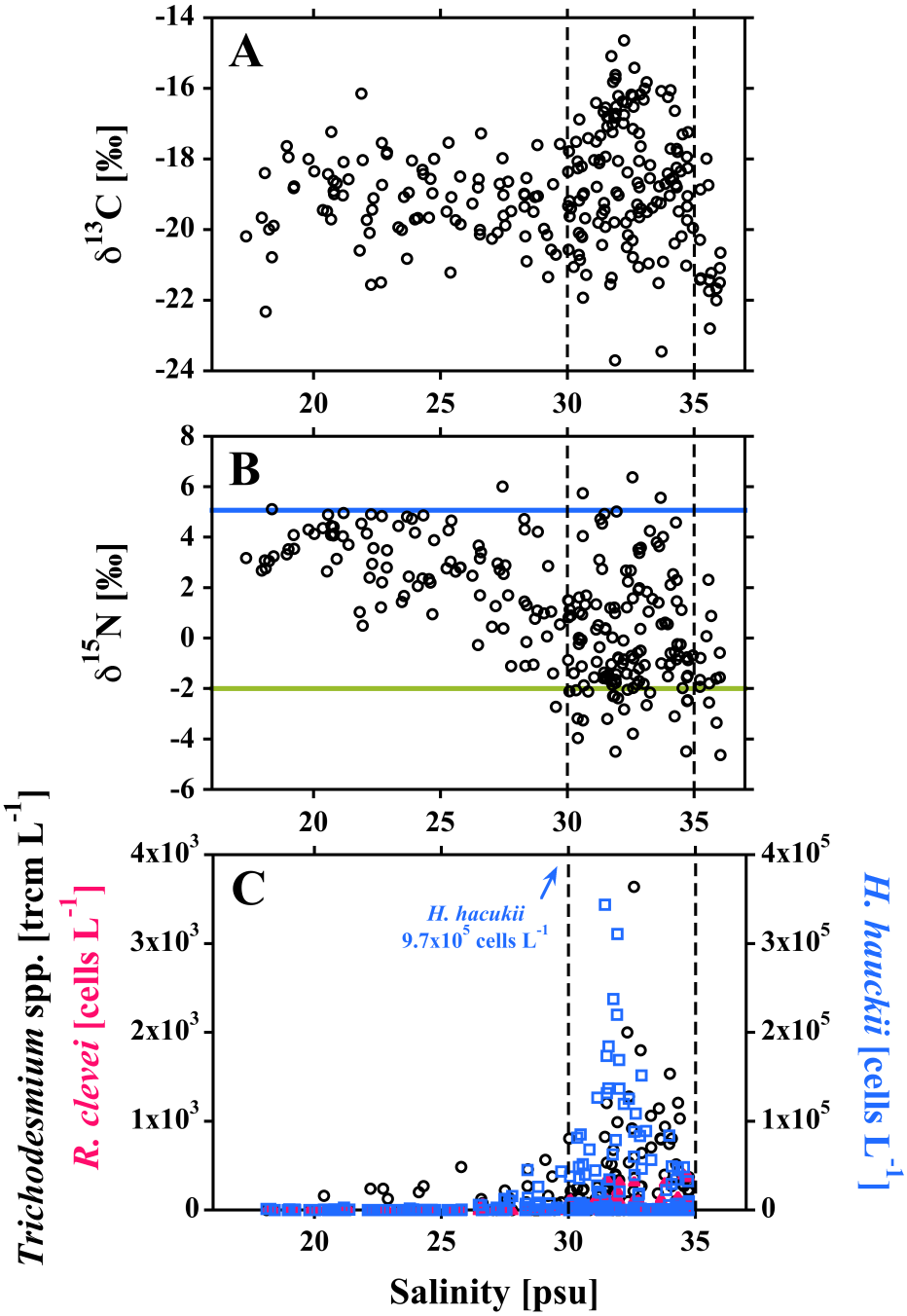

Figure 2.6: $\delta^{13}C$ (**A**) and $\delta^{15}N$ (**B**) of particles as a function of salinity from underway and surface CTD samples. The green and blue lines in (**B**) designate the average $\delta^{15}N$ of riverine organic N and deep NO_3^- (5‰; Sigman et al. 2000), and diazotrophic biomass (-2‰; Montoya et al. 2002), respectively. (**C**) Abundances of *H. hauckii, Trichodesmium* spp., and *R. clevei* as a function of salinity. The maximum abundance of *H. hauckii* ($9.7x10^5$ cells L^{-1}) is off scale. Salinity regions are separated by vertical dotted lines.

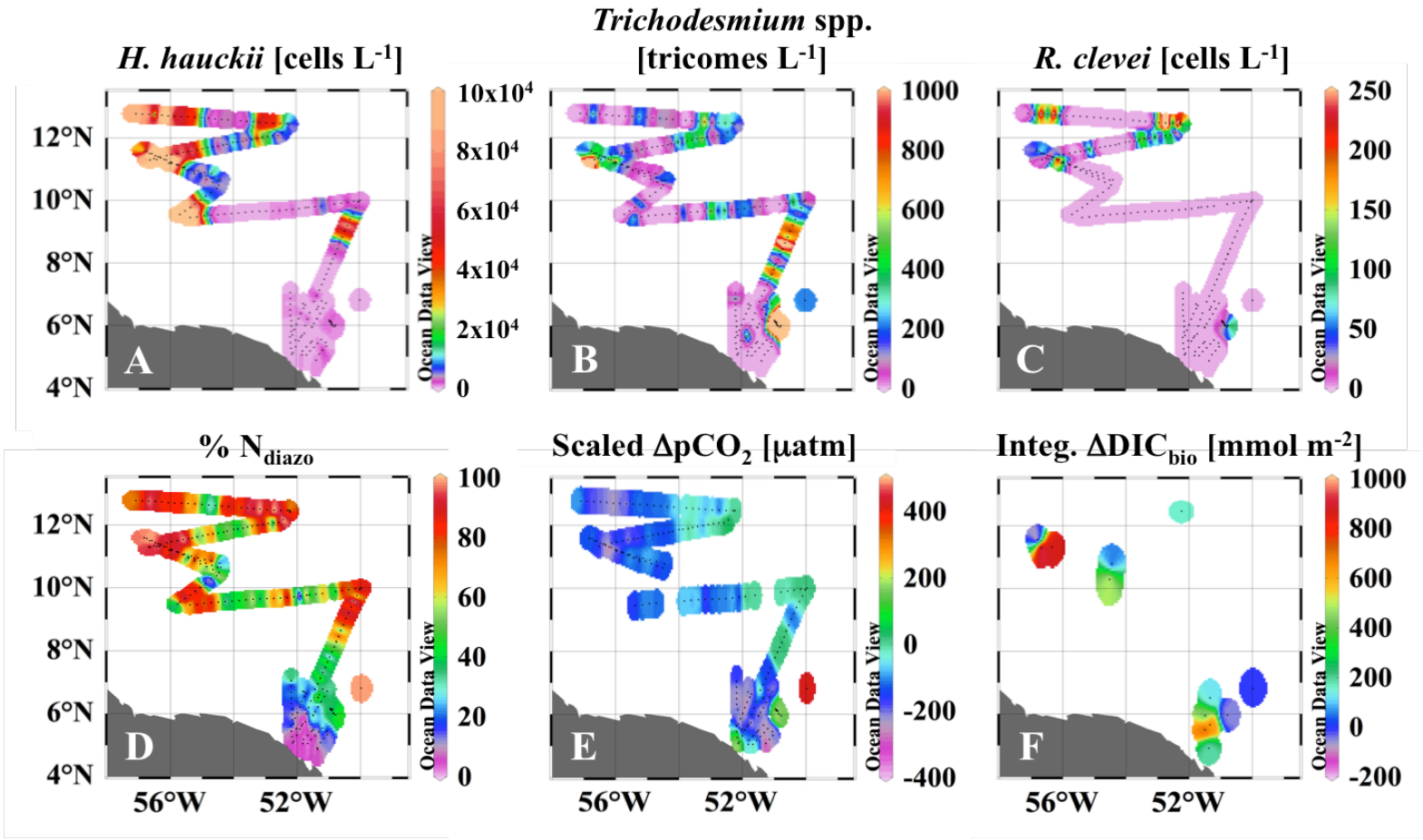

Figure 2.7: Surface distributions of *H. hauckii* (**A**), *Trichodesmium* spp. (**B**), and *R. clevei* (**C**) abundances. Distributions of salinity (**D**), scaled ΔpCO_2 (**E**) and integrated ΔDIC_{bio} (**F**). ΔpCO_2 was scaled to plume thickness using a plume thickness factor (*ptf*; described in *methods*). Integrated ΔDIC_{bio} represents ΔDIC_{bio} integrated through the plume layer.

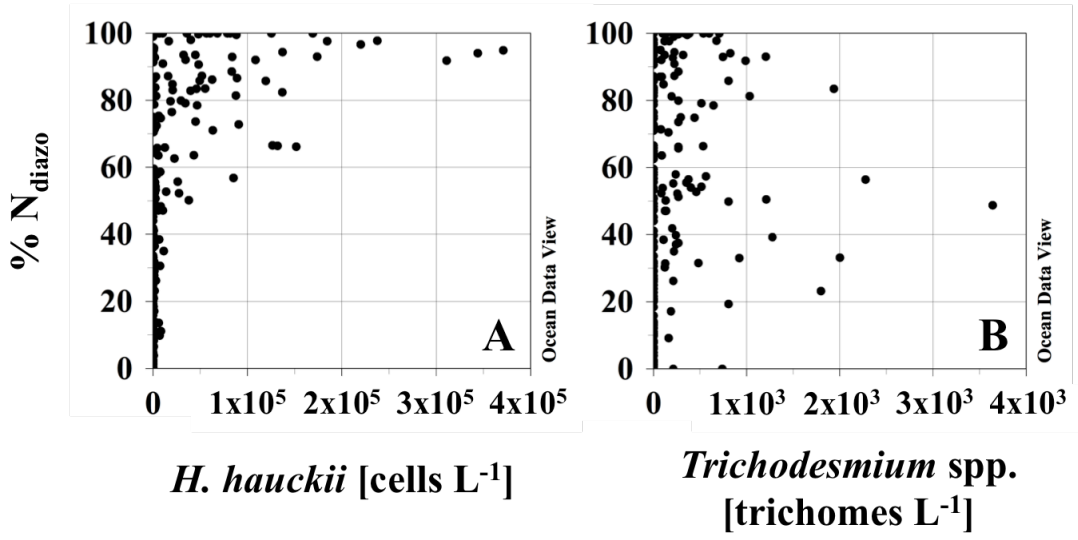

Figure 2.8: Diazotrophic contribution to particulate nitrogen (% N_{diazo}) as a function of *H. hauckii* (**A**) and *Trichodesmium* spp. (**B**) abundances.

2.5 Discussion

The ANACONDAS program builds on previous studies that have characterized the physical (Muller-Karger et al. 1988; Longhurst 1993; Muller-Karger et al. 1995), biogeochemical (Demaster & Pope 1996; Subramaniam et al. 2008), and ecological (Smith & Demaster 1996; Foster et al. 2007; Subramaniam et al. 2008) nature of the Amazon River plume. Our study provides a comprehensive overview of nutrient and particle dynamics in the Amazon plume system during the spring high-flow season when the plume extends to the northwest, transporting surface water to the Caribbean. We document the highly dynamic nature of the Amazon plume system and explore its impacts on coastal and offshore nitrogen and carbon cycles of the Western Tropical North Atlantic.

Our kd490 composite satellite images and underway data (Figs. 2.1 C, 2.2 C) both show that the plume was narrow and coherent in the southern reaches of our cruise track, and broadened and dispersed to the north along the plume axis. We saw sharper transitions to higher salinity waters in the northeastern plume, whereas the northwestern region showed more evidence of lateral mixing. These regional physical differences in the plume have important implications for the distribution of nutrients and functionally diverse phytoplankton communities, as well as their contributions to nitrogen and carbon cycling in the upper water column.

The dynamic nature of the plume is evident in a comparison of plume locations and associated physical properties sampled on both cruise legs. Though coverage on Leg 1 is minimal, it appears that a bolus of very low salinity plume water was injected into the southern region of our survey area within the span of 16 days, shifting the plume

core farther northwest. This shift was accompanied by a large decrease in scaled ΔpCO_2 (-15 vs -150 µatm) and a large increase in integrated ΔDIC_{bio} (-140 vs 900 mmol m^{-2}) in the northern plume region. We also found similar contrasts between Legs 1 and 2 in the southern end of our work area (scaled ΔpCO_2 of -90 vs -230 µatm and integrated ΔDIC_{bio} of 430 vs 560 mmol m^{-2}, respectively). These observations provide evidence of the episodic and dynamic nature of the plume, which creates a patchwork of waters of varying age, physical properties, and biological impact.

2.5.1 Nutrient & Phytoplankton Distributions

Nutrient concentrations ($NO_3^- + NO_2^-$, PO_4^{3-}, and SiO_2) showed marked departures from conservative mixing between riverine and oceanic waters. Nitrate + nitrite was mostly absent from surface waters along our cruise track (Figs. 2.3 A, 2.4 A), in keeping with the results of previous studies (Demaster & Pope 1996; Smith & Demaster 1996), with only a few instances of measurable concentrations in the southern plume core. Phosphate had a much more complicated distribution relative to salinity, with marked deviations from conservative mixing in all salinity regions (Figs. 2.3 B, 2.4 B). Though we found evidence of some PO_4^{3-} drawdown in the southern plume, it appears that conservative mixing was the primary factor shaping PO_4^{3-} distributions below 9˚N (Fig. 2.4 E). In contrast, PO_4^{3-} concentrations increased substantially to the north along the plume axis, leading to strong positive deviations from conservative behavior. Fox et al. (1986) and Berner & Rao (1994) had previously documented this trend farther inshore and found that it was caused by the release of PO_4^{3-} from suspended particles and/or dissolved organic matter within the surface plume, but it appears this phenomenon has not previously been documented so far offshore.

Silicate exhibited the most conservative behavior relative to salinity ($r = -0.958$, $p \leq 0.001$; Figs. 2.3 C, 2.4 C), but still showed negative deviations across all salinity regions (Fig. 2.4 F). Negative SiO_2 deviations were prominent on the western side of the plume, where the large diatom *H. hauckii* was the most abundant ($r = -0.229$, $p = 0.0003$), but the deviations did not correlate significantly with *R. clevei* ($r = -0.061$, $p = 0.399$) or *Trichodesmium* spp. ($r = 0.032$, $p = 0.674$) abundances. There was also substantial drawdown in the southern plume waters, where coastal diatom species dominated the biomass.

The conservative mixing line we calculated for SiO_2 (slope = -2.77; ordinal intercept = 100 μM) was in close agreement with that of Yeung et al. (2012), who calculated a slope of -2.45 and an extrapolated river end-member (0 salinity) concentration of 89 μM. Both of these mixing lines appear to produce conservative estimates of river end-member SiO_2 concentrations relative to a previous study conducted by DeMaster et al. (1996), who extrapolated (from 5 – 10 salinity) a freshwater value of 144 μM. In contrast, extrapolation of our PO_4^{3-} conservative mixing line yields a higher PO_4^{3-} river end-member value (1.0 μM) than the DeMaster et al. (1996) value of 0.7 μM. The release of PO_4^{3-} from suspended particles and/or DOM complicates nutrient dynamics, making it difficult to accurately extrapolate to the river end-member. Since we cannot account for consumption/remineralization processes up-stream of our sampling area or for seasonal variability in riverine nutrient concentrations, we cannot confidently anchor our SiO_2 and PO_4^{3-} mixing lines in 0 salinity waters. However, SiO_2 and PO_4^{3-} measurements from the low salinity southern regions of our survey area

provide a robust end-member for our work, which focuses primarily on offshore waters and processes.

The ambient nutrient concentrations within the surface waters of the plume were all far below the Redfield N:P ratio of 16:1, implying severe nitrogen limitation of the phytoplankton. In addition, Si:P was mostly below the Redfield-Brzezinski value of 15:1 (1985). *H. hauckii* was more closely associated with near-Redfield-Brzezinski Si:P regions than were Trichodes*mium* spp. (not shown), suggesting that *H. hauckii* blooms are dependent on the relative concentrations of SiO_2 and PO_4^{3-}, while the abundance of *Trichodesmium* spp. is regulated primarily by PO_4^{3-} availability. These differences in nutrient requirements are likely one of the main drivers of the strong spatial variations we observed in the abundance of the major phytoplankton groups.

Phytoplankton distributions showed distinct regional trends, as well as clear evidence of niche partitioning in the maximum abundances of diazotrophs. Of the diazotrophic phytoplankton examined in this study, *H. hauckii* DDAs were by far the most abundant numerically (Figs. 2.6 C, 2.7 A), dominating the northwestern mesohaline waters. In contrast, *Trichodesmium* spp. concentrations were highest in mesohaline and oceanic waters to the southeast of the plume (Figs. 2.6 C, 2.7 B). On close inspection, *H. hauckii* was almost always present in areas where we found *Trichodesmium* spp., though *Trichodesmium* spp. usually occurred in higher abundance when *H. hauckii* abundance was very low. These distributions may be a reflection of competition between the two diazotrophs, as *H. hauckii* has a higher intrinsic growth rate than *Trichodesmium* spp. (Foster et al. 2007), and *Trichodesmium* spp. are known to produce a variety of allelopathic compounds capable of inhibiting competitors and predators (Hawser et al.

1992; Capone 2005). *H. hauckii* is also known to directly outcompete *R. clevei*, possibly due to *H. hauckii*'s smaller size (with implications for nutrient uptake; Foster et al. 2007), faster growth rate (Villareal 1989; Villareal 1990), or symbiont availability (Foster et al. 2007), all of which may have contributed to the very low abundances of *R. clevei* we observed in our samples (Figs. 2.6 C, 2.7 C).

2.5.2 Particulate Organic Matter & Stable Isotopes

Particulate carbon and nitrogen concentrations were relatively high in the southernmost or freshest part of our sampling region (Fig. 2.5 A, B), suggesting that at least some of the high particle load may have originated from the Amazon River itself. We also saw slightly elevated C and N concentrations in the northwestern mesohaline waters, corresponding with high *H. hauckii* abundances (Fig. 2.7 A). This reflects the ability of rapidly growing diatoms to produce biomass when nutrients (in this case Si and P) are available, which in turn provides an important source of organic matter to support both the pelagic food web and vertical transport to depth. Particulate C:N ratios were usually above the Redfield value (6.6) in areas with high phytoplankton biomass (Figs. 2.5 C, 2.7 A and B), consistent with the strong nitrogen limitation implied by our nutrient measurements, as well as by our direct rate measurements (discussed elsewhere) and integrative estimates of N_2-fixation derived from isotope budgets.

Our measurements of the natural abundance of ^{13}C and ^{15}N in organic particles provided us with an integrative measure of the major processes influencing C and N cycling in the Amazon plume region. The variation in C isotopes in our data appears to be strongly influenced by large, rapidly growing diatoms, in which CO_2-fixation tends to become diffusion limited, leading to limited expression of the enzymatic fractionation of

carbon isotopes and high $\delta^{13}C$ values in the organic matter formed (Goericke et al. 1994; Laws et al. 1995; Rau et al. 1996). In our data, elevated $d^{13}C$ values in organic matter correlated well with *H. hauckii* blooms ($r = 0.470$, $p \leq 0.001$; Figs. 2.5 D, 2.7 A), in keeping with the effects of size and growth rate on carbon isotopic fractionation.

While C isotopes reflect phytoplankton size and growth rate, N isotopes provide an index for N_2-fixation, with lower $\delta^{15}N$ values indicative of N derived from diazotrophy. Using our isotope-mixing model (Eq. 2.1), we were able to quantify the relative contribution of biologically fixed N to the particulate N pool (% N_{diazo}; Fig. 2.7 D). Diazotrophic contributions were near 100% in the northern mesohaline waters, and interestingly, these maxima in % N_{diazo} tended to coincide with high abundances of *H. hauckii* ($r = 0.377$, $p \leq 0.001$; Fig. 2.8 A), whereas the densest *Trichodesmium* spp. populations were associated with % N_{diazo} values of only ~50% ($r = 0.130$, $p = 0.061$; Fig. 2.8 B). This may partly reflect the difference in maximal population densities, which will limit the potential contribution of diazotroph N to the particle field, but trophic processes may also play an important role in generating this contrast. Carpenter et al (1999) argued that nitrogen fixed by DDAs can readily enter the food web through direct grazing, in contrast to nitrogen fixed by *Trichodesmium* spp., which are grazed by only a small number of zooplankton species. Recent studies have additionally demonstrated the importance of zooplankton grazing in controlling plume-associated DDA populations (Stukel et al. 2014) and in moving DDA-derived N into the planktonic food web (Loick-Wilde et al. 2015). The low $\delta^{15}N$ of particles associated with *H. hauckii* also suggests that diazotrophic N is also likely retained in the upper water column as detritus and as rapidly recycled excreta (especially NH_4^+). Such remineralization processes and NH_4^+

recycling may also explain the very low values of $\delta^{15}N$ (close to -3‰, Fig. 2.6 B; Montoya et al. 2002), which are lower than our diazotrophic end-member (-2‰).

2.5.3 DIC & pCO_2

Surface concentrations of pCO_2 and DIC provide insight into the role of biological processes on the carbon cycle in the WTNA. The distributions of pCO_2 depletion and biological DIC drawdown in our study area were closely associated with coastal phytoplankton and *H. hauckii*, suggesting that these phytoplankton play a key role in shaping carbon cycle dynamics. When ΔpCO_2 was scaled to plume depth, these two phytoplankton groups appeared to have comparable impacts on regional pCO_2 depletion (Fig. 2.7 E). *H. hauckii*'s relative influence on carbon export becomes more apparent when comparing plume-integrated ΔDIC_{bio} between these two regions. Areas to the northwest, which contained the largest *H. hauckii* blooms that we encountered, had the greatest integrated ΔDIC_{bio}, even higher than the southern plume where coastal diatoms dominated (Fig. 2.7 F).

Interestingly, *Trichodesmium* spp. seemed to have little impact on either pCO_2 or DIC drawdown. The disparity in the magnitude of pCO_2 and DIC drawdown between regions associated with *H. hauckii* or *Trichodesmium* spp. is likely a reflection of differential export efficiencies of carbon to depth resulting from dissimilar food web interactions. Our results are in agreement with previous studies, which have shown that mesohaline waters in the spring Amazon River plume are associated with increased surface export of silicate and organic C (Yeung et al. 2012) and higher biological silicate deposition in combination with lower C:N in sediments (Chong et al. 2014).

2.5.4 Regional Variations

Our data provide clear evidence for distinct regional variation in the ecology and biogeochemistry of the spring Amazon River plume. In brief, our sampling area can be divided into southern, northwestern, and northeastern regions. The southernmost region (below 8˚N), which contains the youngest plume waters we encountered on our cruise, was a low-salinity, low-diazotrophy area. Despite very high chlorophyll *a* concentrations, diazotrophs were largely absent and the nutrient budget appeared to be dominated by riverine and deepwater sources, characteristics that are reflected in the high $\delta^{15}N$ and low % N_{diazo} signatures of particulate N. The southern plume was shallow and exhibited sharp horizontal gradients in salinity and SiO_2, indicating a limited impact of mixing with oceanic waters. SiO_2 and PO_4^{3-} were present in high absolute concentrations, but showed a deficit relative to conservative mixing as a result of consumption by coastal phytoplankton. With no $NO_3^- + NO_2^-$ in the surface waters, these coastal species, composed primarily of diatoms, cryptophytes, and green-water *Synechococcus* spp. (Goes et al. 2014), must have placed a strong demand on surface $NO_3^- + NO_2^-$ (Demaster & Pope 1996), producing an N-limited environment. It appears that the phytoplankton communities were in part sustained by subsurface NO_3^- from nearby upwelling at the shelf break (Demaster & Pope 1996; Goes et al. 2014; Loick-Wilde et al. 2015), and contributed to carbon export through classic eutrophication processes (Eppley & Peterson 1979; Lohrenz et al. 1997).

Following the aging river water north along the plume axis, we encountered an increasingly salty and less spatially coherent plume, reflecting the impact of lateral and vertical mixing. Within the plume core, SiO_2 concentrations decreased due to mixing and

consumption (though not to the point of depletion), while PO_4^{3-} concentrations increased, most likely due to release of P from particles and/or DOM. This PO_4^{3-} transport mechanism may further enhance the role of the aging plume as a stimulant of offshore diazotrophy by supplying PO_4^{3-} to SiO_2-rich, $NO_3^- + NO_2^-$ -poor waters, ultimately promoting new biological production and export of carbon to the deep ocean.

Interestingly, regions with nearly identical salinity and nutrient conditions in the northern plume had very different abundances of DDAs and showed evidence of differential biogeochemical impacts of N_2-fixation. This implies that DDA blooms are controlled by other factors in addition to the basic physical/chemical regime within the plume. In particular, exposure time, or habitat duration, must also play a critical role in promoting DDA blooms. Subramaniam et al (2008) and Goes et al (2014) described general habitat preferences of phytoplankton, establishing that the biogeography of communities largely fell along the salinity gradient and was more broadly shaped by $NO_3^- + NO_2^-$ availability, but they did not explicitly consider the role of time. Stukel et al (2014) demonstrated the importance of the temporal dimension in their Amazon River plume DIAZO ecological model and found that retention of DDAs in mesohaline waters for several weeks resulted in bloom formation. Though we lack a direct measurement of water mass age, the spatial extent of a habitat is related to the potential retention time of phytoplankton within it. Due to the very dynamic nature of the plume, larger habitats are associated with longer habitat exposure and ultimately higher densities of DDAs.

This spatiotemporal relationship in bloom formation is clearly evident in the northern plume. For example, we encountered $NO_3^- + NO_2^-$ -depleted, mesohaline waters on the northeastern edge of the plume, but this area was relatively small in size, as the

plume core transitioned quickly to oceanic waters in this area. DDAs were present but at relatively low abundances, and contributions to pCO_2 and DIC drawdown were small. In contrast, the northwestern side of the plume was characterized by large expanses of mesohaline waters, where a physical-biological model (Coles et al. 2013) suggests that mesoscale eddies were the primary driver of mixing. The frequent eddy-induced re-fertilization of NO_3^- + NO_2^- -depleted waters with PO_4^{3-} and SiO_2 generated a sizable DDA habitat. This northwestern region consequently supported the densest DDA blooms encountered during our survey and had a considerable impact on pCO_2/DIC drawdown. Taken together, these data provide strong evidence for the importance of both habitat type and longevity in shaping the regional impact of phytoplankton communities on the nitrogen and carbon cycles of the Western Tropical North Atlantic.

2.6 Conclusion

Recent studies have shown that the Western Tropical North Atlantic is a net sink, rather than a source for atmospheric CO_2 (Subramaniam et al. 2008) and our findings provide critical insight into the processes and organisms that are driving the removal of CO_2 from the upper water column. As part of the multidisciplinary ANACONDAS program, we characterized the distributions of nutrients, particulate organic matter, phytoplankton, and stable carbon and nitrogen isotopes in the Amazon plume region during the spring high-flow period. Our data provide an integrative overview of the impact of the plume on nutrient and elemental cycling as well as the distribution of major groups of diazotrophs. We found clear evidence that the Amazon plume plays a critical role in fertilizing offshore waters, but in a way that promotes diazotrophic growth rather than simple eutrophication. The diazotroph community showed clear regional variation, with strong dominance by DDAs, primarily *H. hauckii*, in the mesohaline waters to the northwest of the plume axis. Though nutrient availability plays a primary role in generating conditions suitable for *H. hauckii* growth, both grazing (Stukel et al. 2014; Loick-Wilde et al. 2015) and the duration of exposure to favorable conditions (Stukel et al. 2014) are important in shaping the finer scale distributions of DDAs in the WTNA.

Our isotope budgets show that the two major diazotrophs in our study area, DDAs and *Trichodesmium* spp., contribute to the food web and to the vertical flux of organic matter in very different ways, though both are significant sources of new production in the plume. Specifically, DDAs appear to make a more direct contribution to the food web, as found by Loick-Wilde et al (2015), which results in a much greater contribution to the overall export flux of carbon in this region (Subramaniam et al. 2008; Yeung et al.

2012). As a result, surface waters associated with DDA blooms are highly depleted in DIC.

Although our work is specific to the Amazon plume region, the limited data available suggest that our findings are relevant to other large river systems that drain into tropical oceans, particularly the Congo (Foster et al. 2009) and the Mekong (Voss et al. 2006). In these and other systems, riverine inputs of nutrients and the processing of nutrients that occurs in the river plume, are likely to promote both diazotrophic activity and consumption of CO_2, with important impacts on the regional and global nutrient and carbon budgets.

CHAPTER 3

HERCULES 265 RAPID RESPONSE: IMMEDIATE ECOSYSTEM IMPACTS OF A NATURAL GAS BLOWOUT INCIDENT[†]

Sarah C. Weber*[1], Leigha Peterson[2], Jessica J. Battles[3], Brian J. Roberts[4], Richard N. Peterson[2], David J. Hollander[5], Jeffrey P. Chanton[6], Samantha B. Joye[3], Joseph P. Montoya[1]

[1] Georgia Institute of Technology, School of Biology, Atlanta GA 30332 USA

[2] Coastal Carolina University, School of Coastal and Marine Systems Science, Conway SC 29526 USA

[3] University of Georgia, Department of Marine Sciences, Athens GA 30602 USA

[4] Louisiana Universities Marine Consortium, Chauvin LA 70344 USA

[5] University of South Florida, College of Marine Science, Tampa FL 33701 USA

[6] Florida State University, Department of Earth, Ocean, and Atmospheric Sciences, Tallahassee FL 32306 USA

[†] Manuscript in press in Deep-Sea Research II

3.1 Abstract

In late July 2013, the Hercules 265 drilling rig in the Northern Gulf of Mexico experienced a catastrophic loss of control. Large quantities of natural gas spewed into the environment for ~2 days before the well self-sealed through down-hole collapse below the seafloor. ECOGIG (Ecosystem Impacts of Oil and Gas Inputs to the Gulf) and collaborating GoMRI (Gulf of Mexico Research Initiative) consortia mounted a rapid response cruise to characterize the waters around the Hercules 265 rig, beginning just 4 days after the blowout. Our analysis showed an immediate microbial response to the elevated concentrations of methane in the water column, as evidenced by the drawdown of oxygen to hypoxic conditions, the incorporation of methane-derived carbon into particles, and measurable rates of methane-assimilation and nitrogen-fixation. Additionally, radium isotope measurements allowed us to constrain the timescale of bottom water exposure to the influence of the rig. A second sampling by the C-IMAGE (Center for Integrated Modeling and Analysis of Gulf Ecosystems) consortium indicated that the ecosystem had returned to near pre-blowout conditions within one month.

3.2 Introduction

Substantial quantities of oil and gas are released into the Gulf of Mexico by natural seeps and through anthropogenic mechanisms involving accidental discharge during the exploration, production, and transportation of hydrocarbons (Anderson et al., 2012) in addition to other commercial activities (Schleifstein, 2013). A variety of studies in the wake of the Deepwater Horizon (DWH) incident in 2010 revealed clear changes in the composition and activity of microbial communities exposed to increased concentrations of oil and gas over extended periods of time (Kessler et al., 2011; Redmond and Valentine, 2012; Crespo-Medina et al., 2014; Joye et al., 2014a). In particular, the microbial consumption of methane was linked to localized depletion of water column oxygen at depth (Joye et al., 2011; Kessler et al., 2011; Yang et al., 2014) and likely facilitated the movement of oil and gas carbon into particles and zooplankton near the shelf (Graham et al., 2010; Chanton et al., 2012; Cherrier et al., 2013). Larger organisms were also affected by the exposure, including a variety of corals (White et al., 2012; Fisher et al., 2014b; Fisher et al., 2014a) and fish (Murawski et al., 2014).

Although the DWH spill has received an unprecedented level of attention from the oceanographic community, much of the scientific effort occurred after the spill was well under way and focused on the longer-term, cumulative effects of the introduction of massive quantities of oil and gas into a pelagic ocean ecosystem. Relatively little is known about the immediate responses of planktonic systems in the early stages of an anthropogenic release of oil and gas.

On the morning of 23 July 2013, the Hercules 265 drilling rig (operated by Walter Oil and Gas Corporation) located in South Timbalier Block 220 in the Northern Gulf of

Mexico (55 miles offshore of Louisiana, Fig. 3.1 A) lost control of one of its wells while performing completion work in preparation for natural gas production (BSEE, 2013). Two hours after the blowout began, the rig caught fire and continued to burn until the well self-sealed two days later (25 July) by natural bridging, or collapse of the well below the sea floor, blocking the flow of natural gas (BSEE, 2013). Aerial surveys conducted by the Bureau of Safety and Environmental Enforcement (BSEE) and the non-profit organization On Wings Of Care (OWOC) indicated that the well had released primarily natural gas, as only a light sheen of oil was seen on the surface during the blowout (BSEE, 2013; Schumaker, 2013). It was assumed that the majority of the gas was expelled to atmosphere via the riser pipe.

Upon receiving word of the blowout, ECOGIG (Ecosystem Impacts of Oil and Gas Inputs to the Gulf) and collaborating consortia established through the Gulf of Mexico Research Initiative (GoMRI) organized a rapid response effort to assess the environmental impact of the Hercules 265 blowout (Joye et al., 2014b). The collaborating consortia included the Gulf of Mexico Integrated Spill Response (GISR), the Center for Integrated Modeling and Analysis of Gulf Ecosystems (C-IMAGE), the Consortium for Advanced Research on Transport of Hydrocarbon in the Environment (CARTHE), and the Coastal Waters Consortium (CWC). Fortuitously, the blowout occurred near the end of a major ECOGIG field effort, so substantial resources were available on short notice. Within four days of the blowout (27 July), consortium scientists were aboard the R/V Acadiana deploying surface drifters, and began sample collection shortly thereafter (29 – 30 July).

This study is the first to explore the immediate impact of a large release of natural gas in a marine shelf environment and provides novel insight into the nature and timescale of the microbial community response to this sort of perturbation. Here we present the hydrographic context of the blowout, the water column distributions of methane and oxygen, and the rates of critical microbial processes in the seven days following the blowout. A subsequent visit to the blowout site roughly a month later provided additional insight into the timescale of recovery from the gas release.

3.3 Materials & Methods

3.3.1 Rapid Response Cruise (27 – 30 July 2013)

Samples were collected and experiments carried out near the Hercules 265 rig (28.384°N, 90.524°W, Fig. 3.1) aboard the R/V *Acadiana*. Four days after the blowout, six sets of Lagrangian surface drifters were deployed at 60° intervals at a distance of 5 nautical miles (NM) from the rig (Stn. 1-6, Fig. 3.1). Drifter trajectories gathered in real time informed the sampling efforts that began two days later. Based on these trajectories, we focused our survey to the SE of the rig, sampling in an arc 1.5 NM away from the rig (the closest the Coast Guard would allow sampling; Stns 10 - 12, 15) and on another arc 5 – 5.5 NM away (Stns 8, 13, 14, 16, 17). Dispersion of the drifters, which were affected by wind as well as water motion, provide an upper limit to mixing and dilution of surface water, which we estimated by comparing the initial area bounded by the drifters (dark orange shading in Fig. 3.2 A) to the bounded area at later time points (Fig. 3.2 B, C).

Water samples and hydrographic data were collected at these nine stations using an SBE 55 CTD and a rosette equipped with six 4 L sampling bottles. To meet water demands with these relatively small bottles, multiple casts (usually 4) were required to cover the entire water column (50 – 60 m depth), with all parameters at a given depth being sampled on the same cast. With the exception of Stn. 8, the R/V *Acadiana* held position for the duration of sampling at each station.

Nutrient samples (NO_3^-, NO_2^-, PO_4^{3-}, SiO_2) were frozen at sea and run within one month of collection using a Lachat QuikChem 8000 flow-injection analysis system. Samples were thawed, equilibrated at room temperature for at least 24 hr and filtered (0.2 μm polycarbonate) prior to analysis. Due to possible bias from particle leaching

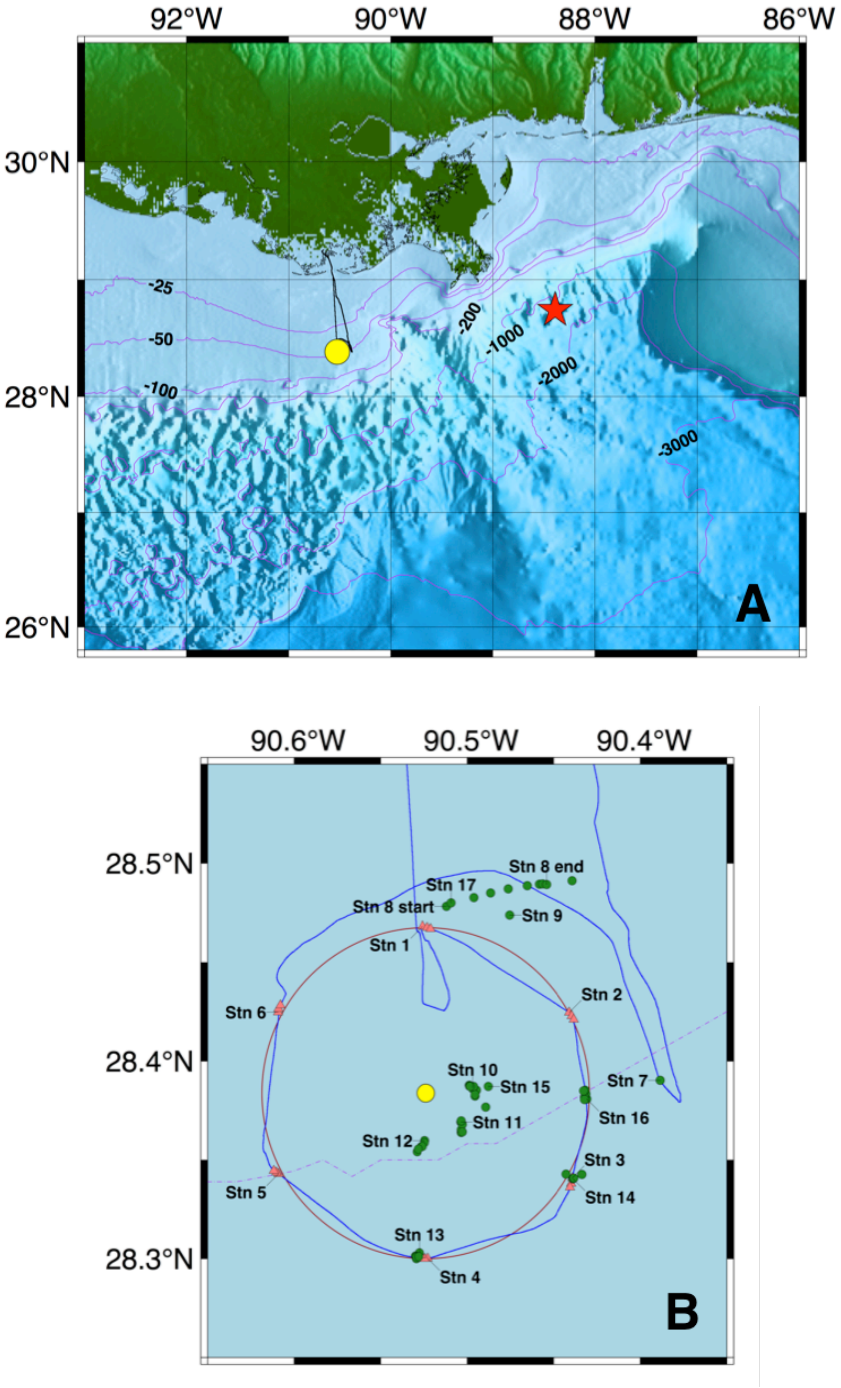

Figure 3.1: (**A**) Chart showing the Mississippi Delta and the locations of the Hercules 265 drilling rig (yellow circle) and the Deepwater Horizon drilling rig (red star). Panel **B** shows the vicinity of the rig (yellow circle), the 50 m isobath (dashed red line), the day 1 cruise track (blue), drifter releases (red diamonds) along the 5 NM radius, and CTD casts (green circles).

using this methodology, these nutrient concentrations can be treated as upper limits. N*, or deviation from Redfield Ratio, was calculated using the method outlined in Gruber & Sarmiento (1997).

Samples for dissolved methane quantification were collected as soon as the CTD rosette was secured on deck (Joye et al. 2011). Concentrations of C1 to C5 alkanes were determined using headspace extraction (Joye et al. 2011): 55 mL of sample was placed into a 75 mL helium-purged serum vial containing one pellet of NaOH to arrest biological activity in the sample by raising the pH. The sample was the mixed and stored refrigerated prior to analysis. To quantify methane concentration, a 1 mL gas phase sub-sample was injected into an SRI 8610c gas chromatograph equipped with a flame ionization detector. Concentrations were calculated by comparison to an aqueous methane concentration calibration curve prepared with a certified gas mix (1% methane in helium Scott Specialty Gases®) and sterile seawater.

These discrete methane measurements were used to calculate the average, depth-weighted concentration of methane in the water column at each station. The average concentrations were calculated by first integrating methane concentration through the depth sampled at each station (weighting by depth) and then dividing this areal concentration by the greatest depth sampled to yield the average water column concentration.

To measure the isotopic composition of CH_4, water samples were injected into evacuated vials and brought to atmospheric pressure with helium and equilibrated. Headspace samples were then injected into a Hewlett Packard gas chromatograph fitted

to a ThermoFinnegan Delta V Isotope ratio mass spectrometer for gas chromatograph–combustion–isotope ratio mass spectrometry (GC-C-IRMS).

Suspended particles were collected by positive-pressure (5 – 10 psi) filtration onto pre-combusted 47 mm GF/F filters. Filters were frozen at sea and then dried ashore at 60^{o}C and stored over desiccant prior to analysis. Nitrogen and carbon elemental and isotopic compositions of suspended particles were measured by continuous-flow isotope ratio mass spectrometry (CF-IRMS) using a Carlo Erba NC2500 elemental analyzer interfaced to a Micromass Optima. All isotope natural abundances are expressed as δ-values relative to atmospheric N_2 ($\delta^{15}N$) and VPDB ($\delta^{13}C$).

To measure radium (Ra) isotopes, the filtrate from our particle sampling (10 – 20 L) from Stations 10 – 16 was passed slowly (~1 L/min) over acrylic fibers impregnated with MnO_2, which quantitatively adsorbs dissolved Ra (Moore & Reid 1973). Initial ^{224}Ra measurements were made ashore using a Radium Delayed Coincidence Counter (Moore & Arnold 1996) and were then repeated after three weeks. The paired measurements allowed us to correct for ^{224}Ra derived from adsorbed ^{228}Th, isolating enrichments resulting from recently discharged subsurface fluids from those produced by *in situ* decay of the parent isotope. ^{226}Ra activities were measured indirectly by quantifying the radioactive ingrowth of its gaseous daughter, ^{222}Rn (222-radon). Produced ^{222}Rn was concentrated using a cold trap on a Rn emanation line (Mathieu et al. 1988) and activities were measured via scintillation in a photomultiplier tube following methods outlined in Peterson et al. (2009).

Water column respiration rates were determined for 2 – 4 depths at Stations 8 and 10 – 15 (total n = 23). At each depth sampled, four 300-mL biological oxygen demand

(BOD) bottles were filled from a single Niskin bottle using tygon tubing, allowing water to overflow the bottle by 2 – 3 volumes and taking care to expel all bubbles from the sample before capping. Half of the bottles were immediately fixed with 1mL each of manganous sulfate and alkaline iodide solutions and half were incubated in the dark at *in situ* temperatures for ~24 hours before being fixed. Once stoppers were placed in each BOD bottle, deionized water was added to fill the flared top and a secondary plastic cap was used to ensure a gas-tight seal. All fixed samples were stored in the dark prior to titrations. Dissolved oxygen concentrations in the initial and final bottles were determined using a modification of the Winkler titration method detailed in Strickland & Parson (1972). Titrations were performed on three to five 50-mL aliquots per bottle using a Mettler Toledo DL28 auto-titrator. The mean and median coefficient of variation in DO concentrations among duplicate initial and final BOD bottles was 1.0% and 0.7%, respectively. Water column respiration rates were calculated as the rate of change in DO over time, expressed as $\mu mol\ O_2\ L^{-1}\ d^{-1}$.

Initial (ambient) DO concentrations measured from the BOD bottles (33 – 286 $\mu mol\ O_2\ L^{-1}$) spanned most of the range of DO concentrations observed in any profile during the sampling campaign. Ambient DO concentrations measured by Winkler titration were not significantly different than CTD measurements of DO ($p = 0.90$; paired t-test) with a mean $DO_{initial} - DO_{CTD}$ of -0.34 $\mu mol\ O_2\ L^{-1}$ (range: -18 to 26 $\mu mol\ L^{-1}$) and a mean $(DO_{initial} - DO_{CTD}) / DO_{initial}$ value of 1.9%, providing a high degree of confidence in the DO patterns observed in CTD profiles.

We conducted experimental incubations to measure rates of N_2-fixation and CH_4-assimilation by transferring seawater to 2.2 L polycarbonate bottles equipped with Teflon

septa. Due to logistical limitations, we could perform only four experiments – one at each of the first four sampling stations (Stns 8, 10, 11, and 12) – using seawater from the deepest depth sampled (34 – 44 m). We conducted triplicate incubations, amending each bottle with 1.0 mL $^{15}N_2$ and 0.05 mL $^{13}CH_4$ following the protocol of Montoya et al. (1996). Bottles were incubated in the dark under simulated *in situ* temperatures for 43 – 52 hours. Experiments were terminated after returning to port by gentle filtration through a 10 μm Nitex prefilter (47 mm diameter) followed by a precombusted 25 mm GF/F filter. Material collected on the 10 μm prefilter was rinsed onto a precombusted 25 mm GF/C filter. All experimental samples were frozen for transport, and then dried at 60˚C for analysis by CF-IRMS. We used the mass balance approach of Montoya et al. (1996) to calculate rates of N_2-fixation and CH_4-assimilation, and used an average $\delta^{13}C$ of -53‰ for water column CH_4 (Fig. 3.5) in our rate calculations.

3.3.2 Repeat Sampling (25 Aug 2013)

Samples were collected near the Hercules 265 site aboard the R/V *Weatherbird* on 25 August 2013 during a cruise carried out by the C-IMAGE consortium. Stations were located 0.2 NM N and SSE, 5 NM SSE, and 10 NM S of the rig. Water samples were collected with a CTD-rosette and were subsampled for measurement of CH_4 concentrations as described by Magen et al (2014).

3.4 Results

3.4.1 Hydrography & Mixing

The Lagrangian drifters deployed four days after the blowout showed a clear influence of tidal currents on the surface waters, generating the oscillatory trajectory of the center of mass seen in Fig. 3.2. The area bounded by the drifters increased roughly 1.5-fold over the first 34 hours (Fig. 3.2 B versus 3.2 A) and 6-fold over 70 hours (Fig. 3.2 C versus 3.2 A). The net southeastern movement of these drifters led us to focus our sampling in this region "down-stream" of the rig.

To assess water interaction timescales around the wellhead, we used radium isotopes as water mass tracers. Bottom water (42 – 53 m) radium activities showed distinct spatial variations within the sampled domain (Fig. 3.3). Activities of the long-lived radium isotope ^{226}Ra (half-life = 1600 years) ranged from 21.0 to 26.5 dpm 100L^{-1}, with the highest activity to the southeast of the rig (Fig. 3.3 A). Peterson et al. (2013) report similar background ^{226}Ra activities in the Gulf of Mexico of around 20.5 dpm 100L^{-1} and have encountered a range of 5 – 35 dpm 100L^{-1} when in proximity to natural seeps. In contrast, activities of the shorter-lived isotope, ^{224}Ra (half-life = 3.63 days), ranged from 3.9 to 12.7 dpm 100L^{-1}, over 70-fold higher than the GoM (Gulf of Mexico) background ^{224}Ra activities of about 0.3 dpm 100L^{-1} (Peterson et al. 2013). ^{224}Ra activity varied strongly with position and was highest in a band extending to the southeast from the wellhead (Fig. 3.3 B).

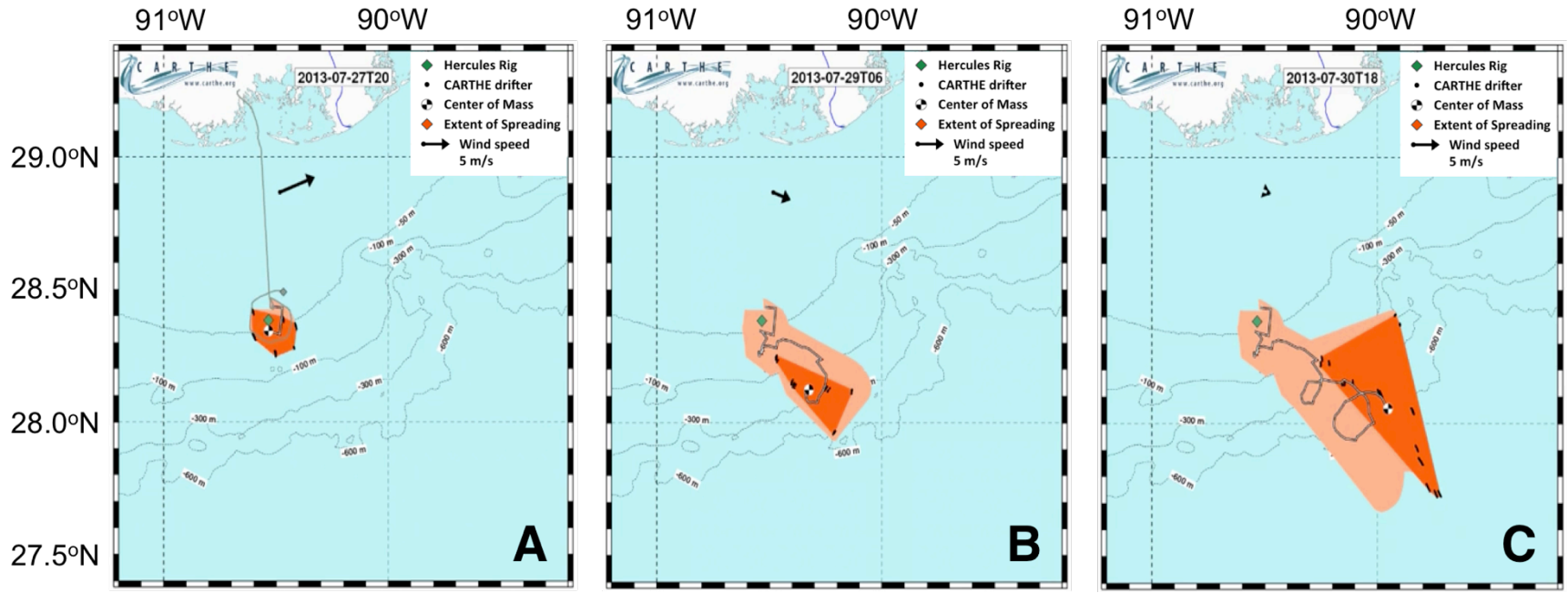

Figure 3.2: Compilation of Lagrangian drifter movements near Hercules 265 immediately after deployment (**A**), 34 hours later at the start of sampling (**B**), and 70 hours after deployment at the end of sampling (**C**). The gray track marks the path of the center of mass and the dark orange shaded region represents the area bounded by the spreading drifters (black dots), while the light orange shading is the cumulative area swept by the drifters since deployment.

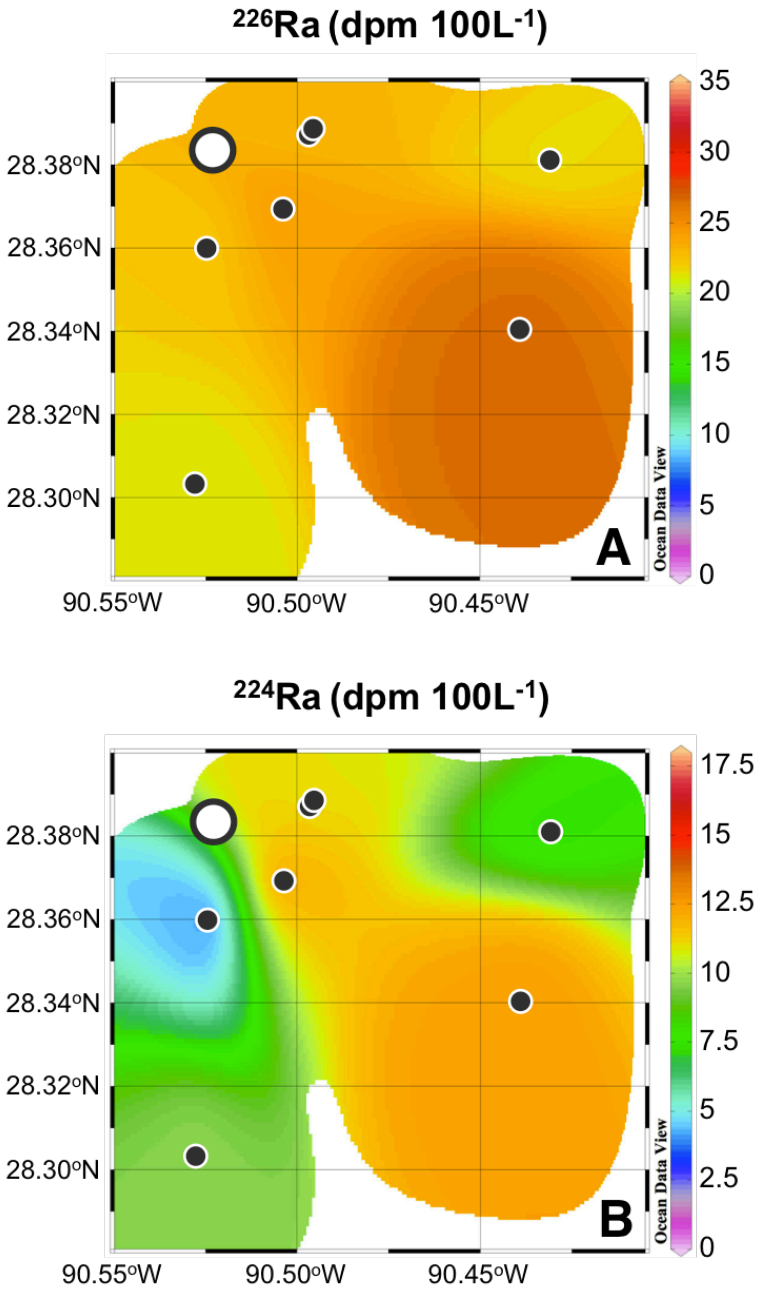

Figure 3.3: Near-bottom water distributions of ^{226}Ra (half-life = 1600 years; (**A**) and ^{224}Ra (half-life = 3.63 days; (**B**) activities. White circle marks the rig position and black circles mark the stations sampled.

3.4.2 Dissolved Species

One of the most striking features associated with the blowout was two distinct layers of hypoxic water (< 62.5 μmol L^{-1}) centered around 25 and 37 m depths at most stations (Fig. 3.4 A; discussed later in context of the Mississippi River "Dead Zone"). When present, the upper layer was generally more depleted in oxygen (43.0 ± 15.3 μmol L^{-1}) than the lower layer (61.9 ± 6.8 μmol L^{-1}). The upper hypoxic layer was not present at the two stations located 1.5 NM (Stn. 12) and 5 NM (Stn. 13) to the south of Hercules 265, whereas the lower layer was present at all stations, though its depth increased in a southward or down-shelf direction from the rig. Total observed oxygen concentrations ranged from 22 – 351 μmol L^{-1} and surface waters were supersaturated with oxygen at all stations, with deeper regions of supersaturation at stations 12 – 15.

Silicate, nitrate + nitrite, and phosphate all showed similar distributions with depth (Fig. 3.4 D, 3.4 E, and 3.4 F). Concentrations were low in the surface waters (0.8 – 7.4 μmol L^{-1} SiO_2, 0 – 8.5 μmol L^{-1} NO_3^-+NO_2^-, and 0.2 – 0.8 μmol L^{-1} PO_4^{3-}) but increased within the upper hypoxic zone (23.9 – 37.4 μmol L^{-1} SiO_2, 13.5 – 18.0 μmol L^{-1} NO_3^-+NO_2^-, and 1.3 – 2.9 μmol L^{-1} PO_4^{3-}) before dropping slightly near the bottom. Nitrite was detectable within the upper 15 m of the water column with a maximum of 0.9 μmol L^{-1} to the north of the rig (data not shown). Most samples showed N:P ratios below the Redfield Ratio of 16:1, resulting in negative N* (deviation from Redfield) values throughout the water column (Fig. 3.4 G), with the most negative values (-24 to -13) occurring at mid-depths in association with low O_2 concentrations.

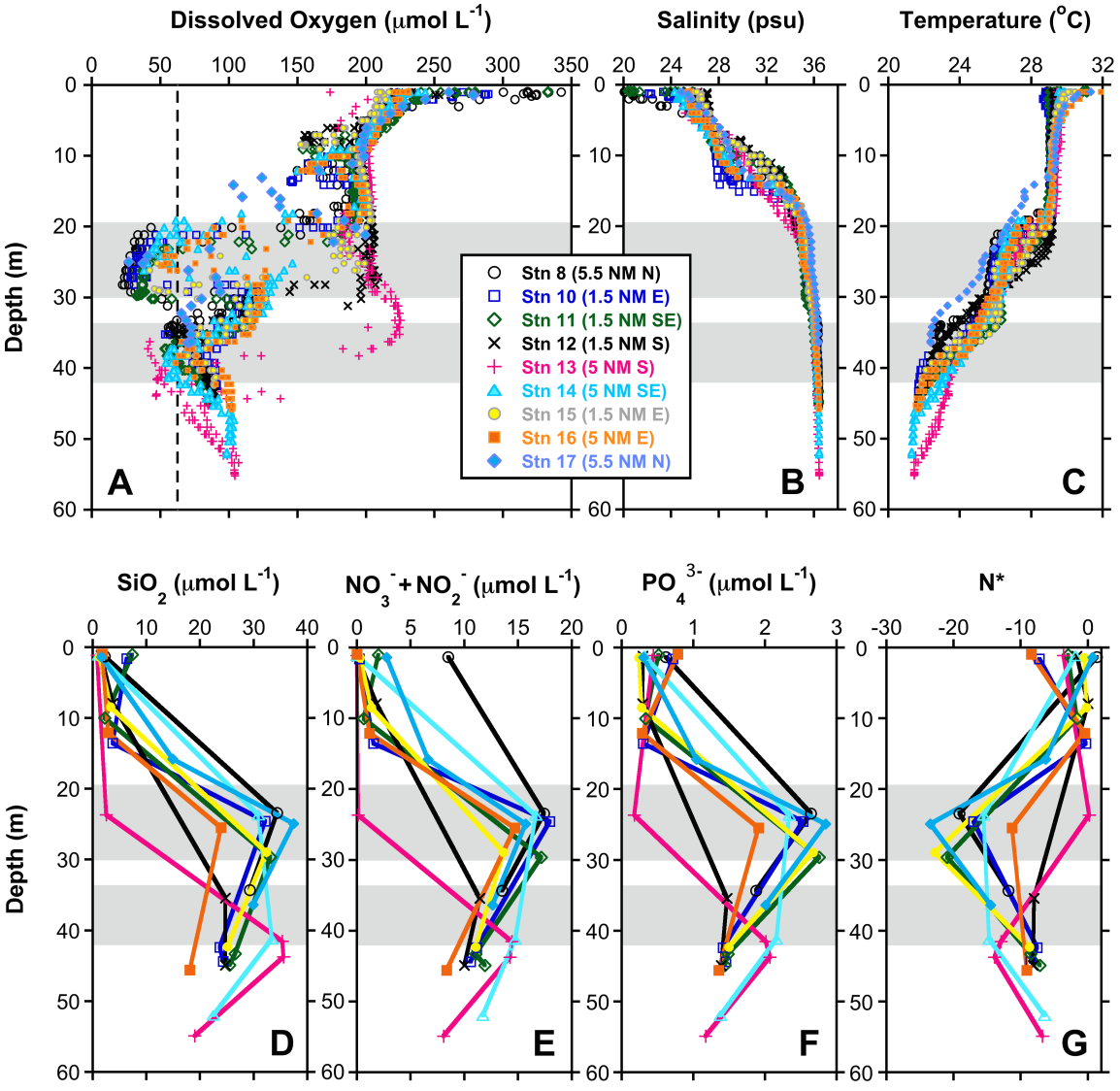

Figure 3.4: Water column properties: (**A**) Vertical distribution of O_2 in the water column. O_2 concentrations tended to be lowest in the two distinct layers marked by the horizontal gray bars, and values left of the vertical dashed line (62.5 µmol L^{-1}) are below the standard threshold for hypoxic. Vertical distributions of salinity (**B**), temperature (**C**), concentrations of SiO^2 (**D**), NO^{3-} + NO^{2-} (**E**) and PO_4^{3-} (B), and distribution of N* (**G**) with depth.

Methane concentrations ranged from 22 – 98 nmol L^{-1} (Fig. 3.5 A) and were elevated considerably above both atmospheric equilibrium (~3 nmol L^{-1}; Scranton & Brewer 1977) and previously reported values for GoM shelf waters (27 ± 5 nmol L^{-1}; Bugna et al. 1996). We found no significant relationship between methane concentration and either depth or distance from the wellhead, whereas the $\delta^{13}C$ of methane did show distinct variation with depth (Fig. 3.5 B). Methane was isotopically enriched (-42 to -31‰) in the hypoxic layers compared to methane in the upper 30 m (-55 to -51‰), but there was no significant relationship between methane $\delta^{13}C$ and methane concentration.

3.4.3 Suspended Particles

The $\delta^{13}C$ and $\delta^{15}N$ of suspended particles ranged from -23.4 to -18.6‰ and 5.7 to 9.7‰, respectively (Fig. 3.6 A, B). All stations displayed similar patterns in $\delta^{13}C$ with depth, with the most negative $\delta^{13}C$ values usually occurring in the hypoxic layers, where values were significantly lower (by roughly 1 – 3‰) than in the surrounding seawater (Spearman $\rho = 0.402$, $p = 0.015$). In contrast, the $\delta^{15}N$ profiles of most stations had maxima within the hypoxic layers with minima centered at about 10 m depth. The C:N ratio of the particles varied little and was close to the Redfield Ratio (6.6:1) throughout the water column.

3.4.4 Rate Measurements

Respiration rates varied widely both with depth and among stations (range: 1.1 – 35.6 μmol O_2 L^{-1} d^{-1}, mean: 11.2 μmol O_2 L^{-1} d^{-1}). In general, respiration was highest near the surface and lowest in the midwater hypoxic layers (Fig. 3.7 A), with a clear

positive relationship with ambient O_2 concentrations over the entire observed range (Fig. 3.7 B).

We measured modest but significant rates of CH_4-assimilation and N_2-fixation into particulate matter at depth (34 – 44 m) around the natural gas rig using $^{13}CH_4$ and $^{15}N_2$ tracer experiments (Fig. 3.8). Water for these experiments was collected from the deepest depth sampled at the first four full stations (Stns 8, 10, 11, and 12), where oxygen concentrations ranged from 57.2 – 90.3 μmol L^{-1}. CH_4-assimilation and N_2-fixation rates ranged from 11.9 to 38.9 nmol L^{-1} d^{-1} and 0.1 to 0.4 nmol L^{-1} d^{-1}, respectively, and the highest rates were measured at Stn. 8 (5.5 NM N of the rig) where dissolved oxygen was lowest (57.2 μmol L^{-1}).

3.4.5 Inter-cruise Comparison

One month after the blowout, the water column was no longer hypoxic and methane concentrations had decreased considerably. The lowest measured O_2 concentration was 94 μmol L^{-1} in bottom waters 0.2 NM from the wellhead, and values fluctuated between 130 – 200 μmol L^{-1} below the surface at the other sites (Fig. 3.9 A). Methane concentrations ranged from 10 – 36 nmol L^{-1} (Fig. 3.9 B), similar to background values for shelf waters (Bugna et al. 1996), and with substantially less heterogeneity in profiles between stations than was observed immediately following the blow out. Atmospheric methane concentrations measured upwind of the bow while heading toward the well were not different from typical ambient values (1.8 ppmv).

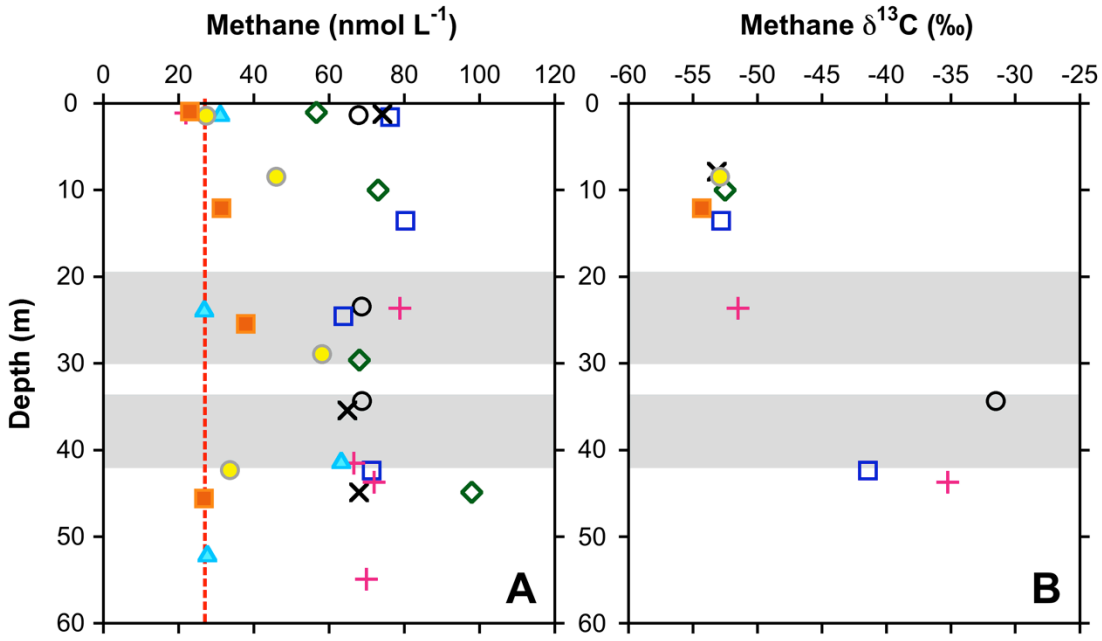

Figure 3.5: Concentration of methane with depth (**A**). The red dashed line marks previously reported background concentrations for GoM shelf waters (27 ± 5 nmol L-1; Bugna et al. 1996). Vertical distribution of methane $\delta^{13}C$ (**B**). Note that methane $\delta^{13}C$ was measured at only a subset of stations and depths. Horizontal gray bars designate commonly hypoxic regions. Symbols as in Fig. 3.4.

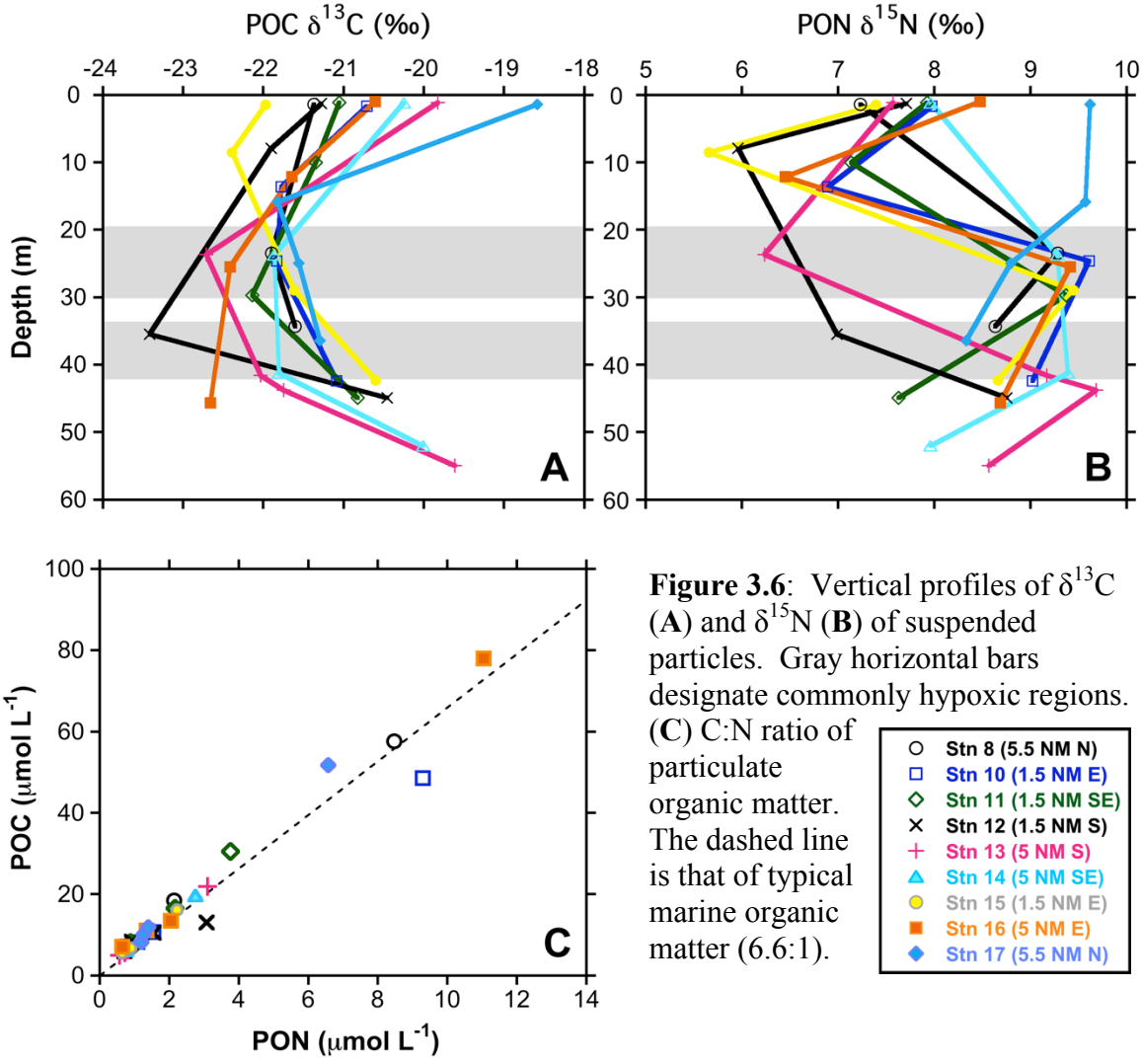

Figure 3.6: Vertical profiles of $\delta^{13}C$ (**A**) and $\delta^{15}N$ (**B**) of suspended particles. Gray horizontal bars designate commonly hypoxic regions. (**C**) C:N ratio of particulate organic matter. The dashed line is that of typical marine organic matter (6.6:1).

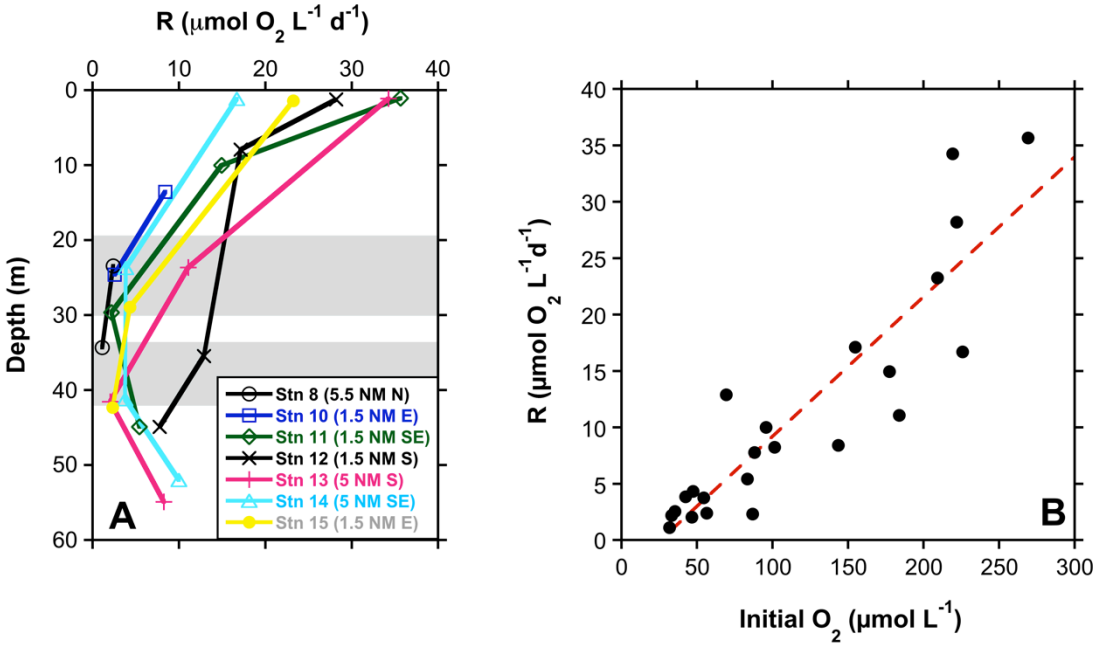

Figure 3.7: Respiration rate as a function of depth (**A**). Gray horizontal bars designate hypoxic layers observed during this cruise. Respiration rate as a function of initial O_2 concentration (**B**). Red dashed line is the least-squares linear regression ($r^2 = 0.87$, $p < 0.0001$).

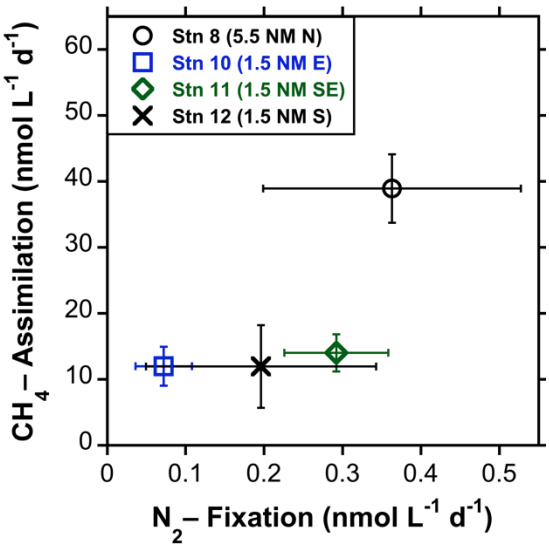

Figure 3.8: Rates of CH_4-assimilation relative to rates of N_2-fixation into particulate matter. Samples were taken from 34 – 44 m depth. Error bars represent standard error of triplicate measurements.

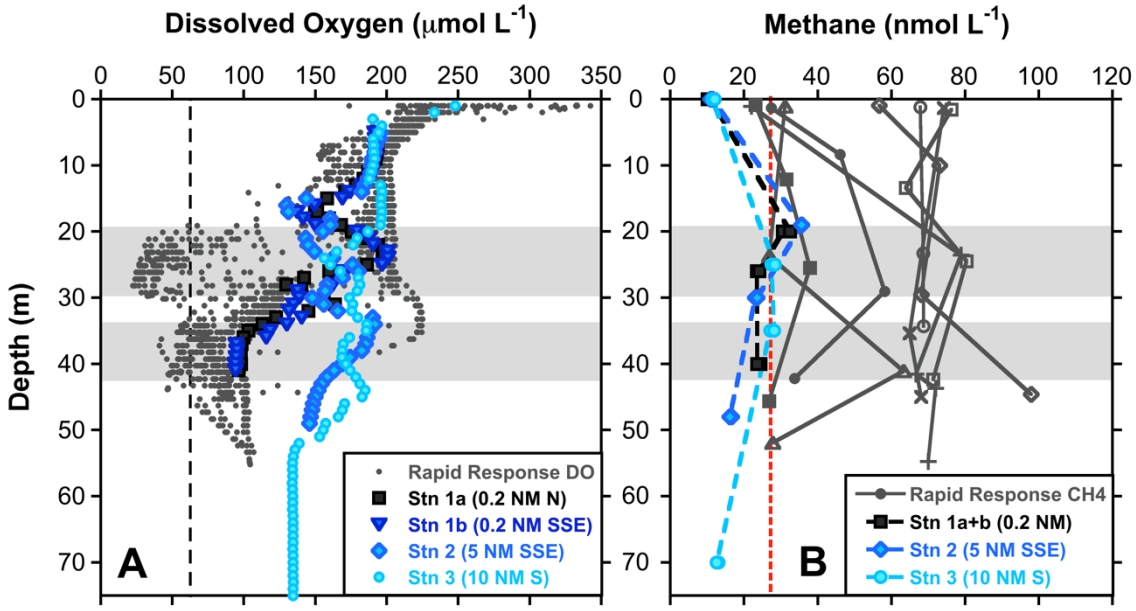

Figure 3.9: Comparison of dissolved oxygen (**A**) and methane (**B**) concentrations from the R/V *Weatherbird* cruise one month after the blowout to those measured during the rapid response cruise 6 – 7 days post-blowout. Background methane concentrations in GoM shelf waters have previously been reported as 27 ± 5 nmol L^{-1} (Bugna et al. 1996; red dashed line in panel **B**).

3.5 Discussion

The blowout of the Hercules 265 rig provided a unique opportunity to study the impacts of a large release of gas, accompanied by poorly constrained quantities of oil, on microbial communities and biogeochemical processes in a shelf ecosystem. To understand the immediate impact of this blowout event, the approximate residence time of seawater around the rig must be established.

3.5.1 Hydrography & Residence Time

The trajectories of the Lagrangian drifters provided real-time information on the strong tidal and inertial motions of the surface waters after the blowout (Fig. 3.2). The 6-fold dilution after 70 hours reflects wind forcing as well as water movement, and is therefore an upper limit on the actual impact of dilution, which clearly played a significant role in dispersing material in the surface waters near the wellhead. The dynamics of water below the pycnocline were at least partially decoupled from the surface layer, so we used radium isotope ratios to estimate the residence time of subsurface water in our study area.

Radium is derived from the decay of parent elements uranium and thorium in shallow sediments and aquifers, and is known to associate with submarine groundwater (Moore 2000; Peterson et al. 2008) and formation fluids (Bloch & Key 1981; Kraemer & Reid 1984), and has also been linked directly to discharge from natural hydrocarbon seeps in the Gulf of Mexico (Peterson et al. 2013). The radium isotopes reported here (^{224}Ra and ^{226}Ra) have very different half-lives (3.63 days and 1600 years, respectively), allowing us to assess differences in relative water mass age on the order of days.

The discharge of groundwater locally may also inject radium isotopes into bottom waters, but the distinct relative activities of ^{224}Ra and ^{226}Ra in groundwater distinguish this input from other sources. Terrestrial groundwaters in the Mississippi River delta contain relatively low activities of the shorter-lived Ra isotopes but elevated activities of the long-lived ^{226}Ra (Krest et al. 1999), whereas hydrocarbon seeps at other sites in the Gulf have been shown to contribute significant ^{224}Ra but little to no additional ^{226}Ra (Peterson et al. 2013). In our study area, bottom water ^{226}Ra activities were uniformly near background Gulf of Mexico levels, while we observed strong enrichments in the short-lived ^{224}Ra near the Hercules 265 rig. These enrichments are consistent with focused inputs via leakage of deeply-sourced, hydrocarbon-bearing fluids from the wellhead.

We used the distribution of Ra isotopes as an index of water mass *relative apparent* age (time since injection of Ra), as well as the impact of mixing within our study area. To estimate age, we first normalized ^{224}Ra activity to ^{226}Ra activity, using ^{226}Ra as an effectively stable tracer on the time scale of interest due to its long half-life (1600 years). The activity ratio (AR = ^{224}Ra: ^{226}Ra) then provides a measure of the apparent age of a water sample relative to the sample with the highest AR (Stn. 10, 1.5 NM E; Fig. 3.10 A). Estimating the absolute time since injection of Ra would require knowledge of the Ra isotopic composition of the source end members (Moore 2000). Relative to Station 10, the time since injection of Ra in bottom waters was less than 1.5 days at the majority of stations.

Interestingly, the relative ages are quite similar to the length of time it took us to sample these waters. If we plot the Ra-derived ages against elapsed sampling time

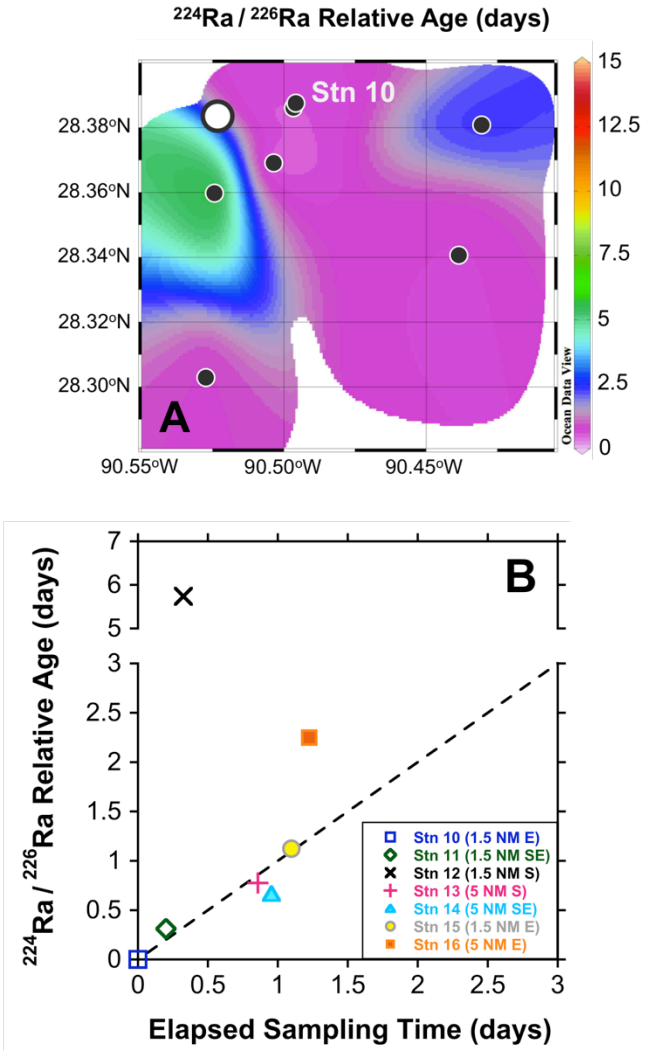

Figure 3.10: (**A**) $^{224}Ra/^{226}Ra$ derived apparent age of bottom water (42 – 53 m) relative to water with the highest activity ratio (Stn. 10, 1.5 NM E). The white circle marks the rig position. (**B**) Relationship between $^{224}Ra/^{226}Ra$ relative age and elapsed sampling time, both relative to Station 10. The dashed line represents a 1:1 relationship between relative age and elapsed sampling time. Note the break in the y-axis.

(Fig. 3.10 B), we find that all but Stations 12 and 16 fall along the 1:1 line. This relationship indicates that at most stations, sampling time alone can account for differences in Ra-derived relative ages. At Stations 12 and 16, however, another process must be acting to increase the apparent ages. Dilution by ambient ocean water ($^{224}Ra/^{226}Ra = 0$) will lead to an overestimate of apparent age, as it will have a minimal impact on ^{226}Ra activity while diluting that of ^{224}Ra. We estimated the dilution of local water by ambient ocean water as:

$$\% \text{ Dilution} = 100 \cdot \left(1 - \frac{^{224}\text{Ra}/^{226}\text{Ra Relative Age}}{\text{Elapsed Sampling Time}}\right) \quad [3.1]$$

yielding dilution estimates of 94% and 46% for stations 12 and 16, respectively. Ultimately, the radium-derived relative ages show that a large portion of our study area to the SE of the wellhead did not experience appreciable dilution or advection during the 1.5 days of sampling (unlike the surface waters), and importantly suggests that deep water in this region interacted with the wellhead over an extended period of time.

3.5.2 Dissolved Species

The difference in dilution/advection (essentially exposure time) between surface and deeper water around the Hercules rig has important implications for the distribution of dissolved species in the water column. One of the more prominent water column features observed during our survey was the two distinct layers of very low oxygen concentrations around the rig (Fig. 3.4 A). Low oxygen concentrations commonly occur near our study area in the Mississippi River "Dead Zone," which has typically remained well north of the Hercules 265 rig location (Rabalais et al. 2007). During larger seasonal events (e.g., 2008), hypoxia has been found to extend farther south (Rabalais et al. 2010),

but the 2013 “Dead Zone” was modest in size and did not extend to our sampling area (NOAA 2013). Thus, the hypoxic layers we observed appear to be directly associated with the blowout and not encroachment of the “Dead Zone”.

Although the "Dead Zone" boundary was well to the north of the Hercules rig, our isotopic and nutrient measurements suggest that shelf waters influenced our study area, particularly in the upper hypoxic layer. Specifically, this upper layer was characterized by very negative N* values (-24 to -13, Fig. 3.4 G) and high particulate $\delta^{15}N$ values (8.6 to 9.7‰, Fig. 3.6 B), both of which are consistent with nitrogen-loss via denitrification and the incorporation of the residual ^{15}N-enriched NO_3^-/NO_2^- into biomass (Voss et al. 2001; Montoya & Voss 2006; Montoya 2008). Though denitrification can be associated with methane oxidation (Modin et al. 2007), it is unlikely that the blowout fostered high local rates of water column denitrification given the relatively high concentrations of oxygen in the hypoxic layers, indicating that these isotopic signatures likely originated elsewhere.

Bottom water O_2 measurements from the Gulf Hypoxia cruises provide important context for exploring the development of the hypoxic layers. The R/V *Pelican* measured a bottom water O_2 concentration of 158 μmol L^{-1} at a station 8.5 NM to the north of the Hercules rig on 23 July, the same day as the blowout. This was substantially higher than the O_2 concentration within our upper (43 ± 15 μmol L^{-1}) and lower (61 ± 8 μmol L^{-1}) hypoxic layers and represents the best estimate we have for the preformed O_2 deficit in this layer. We can use the community respiration rates measured on our expedition to calculate the time needed to reduce the O_2 concentration from our estimate of pre-blowout conditions (158 μmol L^{-1}) to the average values of the post-blowout hypoxic

layers, treating the upper and lower layer averages (43 and 61 μmol L^{-1}, respectively) as a range estimate. The rate of respiration (R) scaled linearly with initial O_2 concentration, which is consistent with O_2 limitation of respiration (Fig. 3.7). Given this relationship, we can use the average R between the pre- and post-blowout O_2 concentrations to estimate the average rate of respiration between the blowout and our sampling, and therefore the time required to draw down O_2 to the low levels we observed. An average R of 8.9 – 10.3 μmol L^{-1} d^{-1} could produce the observed hypoxia in roughly 10 – 13 days, which is longer than the time between the blowout and our sampling (~ 6 d). Higher initial respiration rates immediately after the blowout and other secondary processes, such as the physical sparging of oxygen from the water column by the released natural gas, may have enhanced oxygen depletion and could account for this discrepancy.

Methane concentrations and isotopic signatures provide further support for the local origin of the methane and the limited influence of "Dead Zone" waters in this region. Most of the CH_4 released during the blowout was thought to have vented directly to atmosphere through the riser pipe, but our dissolved CH_4 measurements (22 – 98 nmol L^{-1}; Fig. 3.4 D) were elevated relative to both previously reported background values (27 ± 5 nmol L^{-1}; Bugna et al. 1996) and those measured on the R/V *Weatherbird* a month later (Fig. 3.9). This is evidence that significant quantities of CH_4 must have dissolved directly into the water column. The $\delta^{13}C$ of this dissolved methane (-55 to -31‰, Fig. 3.5) additionally implies that it was predominantly of thermogenic origin ($\delta^{13}C$ generally > -50‰; Hoefs 1987), indicating that this methane was injected from the wellhead, as opposed to having been advected in from the "Dead Zone" where biogenic

methane ($\delta^{13}C$ generally < -60 ‰; Hoefs 1987) is known to accumulate from methanogenic activity (Naqvi et al. 2010).

The distinct trends in the vertical distribution of methane $\delta^{13}C$ also reveal interesting dynamics in the dissolved methane pool (Fig. 3.5). If the relatively low $\delta^{13}C$ of methane nearer the surface (-55 to -51‰) is isotopically representative of the source, then the ^{13}C enrichment of methane at depth (-42 to -31‰) likely reflects isotopic fractionation during assimilation by bacteria/archaea (Barker & Fritz 1981) . If we apply a simple closed-system fractionation model:

$$\delta_{\mathrm{RS}} = \delta_{\mathrm{INPUT}} - \Delta \cdot ln(1 - f) \qquad [3.2]$$

we can estimate the fraction of methane (*f*) that would have to be consumed to generate this isotopic difference, where δ_{RS} is the natural abundance of the residual substrate (-33‰), δ_{INPUT} is that of the initial substrate (-53‰), and **Δ** is the fractionation factor associated with CH_4 assimilation. Using a conservative value of -13‰ for **Δ** (Jahnke et al. 1999), we estimate that ~73% of the dissolved methane within the hypoxic layers was consumed.

We can then constrain the initial CH_4 concentrations in the deep water near the rig by applying this uptake fraction to our final (observed) CH_4 concentrations. Averaging the methane concentrations of the samples where $\delta^{13}C$ of deep CH_4 was measured (Stations 8, 10, and 13; Fig. 3.5) gives us ~70 nmol L^{-1} CH_4, which equates to an initial concentration of ~260 nmol L^{-1}. Interestingly, if we apply our highest methane assimilation rate (~40 nmol L^{-1} d^{-1}) over 4 – 5 days (time since the well self-sealed, "closing" the system), we can account for the uptake of 160 – 200 nmol L^{-1} methane, which is in general agreement with the results of the fractionation model. This finding

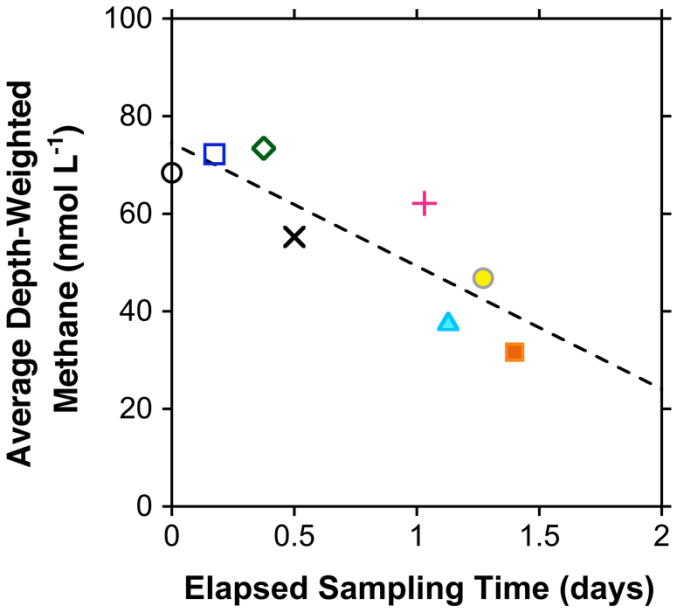

Figure 3.11: Depth-weighted methane concentrations (nmol L^{-1}) averaged by station versus elapsed sampling time (days). Dashed black line is the linear regression ($r^2 = 0.73$, $p = 0.0072$). Symbols as in previous figures.

provides us with two important insights: (1) methane was no longer being supplied in significant quantities to the system (at depth) since this uptake fractionation signal would otherwise be obscured, and (2) the uptake of methane appears to be strongest within the hypoxic layers (though measurements are limited in the upper layer).

Surprisingly, we found no correlation between CH_4 concentration and distance from the rig, but we did find a distinct negative relationship between station average methane concentration and elapsed time (Fig. 3.11; see methods for details). Although our data imply that different processes shaped the methane distributions through the water column, the change in average station methane concentrations through time suggests that dilution/advection in the surface waters and consumption at depth were the major processes reducing methane concentrations through time.

3.5.3 Particulate Organic Matter & Rates

The depletion of ^{13}C in suspended particles within the hypoxic layers is also consistent with the incorporation of CH_4-carbon into the food web, as observed by Cherrier et al. (2013; see also Fig. 3.8 A). Though this low $\delta^{13}C$ signal could also reflect inputs of terrestrial plant carbon delivered by the Mississippi River ($\delta^{13}C \approx -26‰$; Kendall et al. 2001), the C:N ratio of the particles is uniformly similar to that of marine organic matter (6.6:1, Fig. 3.6 C), not of terrestrial plant matter, which is typically > 20 (Kendall et al. 2001). If we assume that the only two significant sources of isotopically distinct carbon in the particles are (1) CH_4 from the Hercules 265 rig and (2) average marine organic matter, we can use a simple isotope budget to estimate the contribution of CH_4 to biomass (particles) around the rig:

$$\delta^{13}\mathrm{C}_{\mathrm{Obs}}[\mathrm{POC}]_{\mathrm{Obs}} = \delta^{13}\mathrm{C}_{\mathrm{CH_4}}[\mathrm{POC}]_{\mathrm{CH_4}} + \delta^{13}\mathrm{C}_{\mathrm{Mar}}[\mathrm{POC}]_{\mathrm{Mar}} \quad [3.3]$$

where subscripts identify the measured values for observed bulk particles (Obs), the portions of the particle field derived from marine organic matter (Mar), and assimilation of CH_4 from the blowout. Since

$$[\mathrm{POC}]_{\mathrm{Obs}} = [\mathrm{POC}]_{\mathrm{CH_4}} + [\mathrm{POC}]_{\mathrm{Mar}} \quad [3.4]$$

we can estimate the contribution of CH_4-derived carbon required to account for the depletion in ^{13}C we observed within the hypoxic layers:

$$[\mathrm{POC}]_{\mathrm{CH_4}} = \frac{\left(\delta^{13}\mathrm{C}_{\mathrm{Obs}} - \delta^{13}\mathrm{C}_{\mathrm{Mar}}\right)[\mathrm{POC}]_{\mathrm{Obs}}}{\delta^{13}\mathrm{C}_{\mathrm{CH_4}} - \delta^{13}\mathrm{C}_{\mathrm{Mar}}} \quad [3.5]$$

where $\delta^{13}C_{Obs}$ and $[POC]_{Obs}$ are the average observed particulate organic carbon $\delta^{13}C$ (-22‰) and concentration (8.5 μmol L^{-1}) within the hypoxic layers, $\delta^{13}C_{CH4}$ (-53‰) and POC_{CH4} represent methane-derived POC, and $\delta^{13}C_{Mar}$ is the typical isotopic signature of marine organic matter (-20‰; Fry & Sherr 1984).

The roughly 2‰ depletion in ^{13}C of suspended particles within the hypoxic layers requires the incorporation of ~515 nmol L^{-1} of methane-derived carbon. We can use our direct measurements of CH_4-assimilation rates to assess the potential for this process to account for the observed isotopic depletion within the hypoxic layers (though our measurements were made with deeper water). Our highest measured CH_4-assimilation rate (~40 nmol L^{-1} d^{-1}, Fig. 3.8 A) acting over six days would lead to the incorporation of ~240 nmol L^{-1} of CH_4, or about half of that necessary to account for the 2‰ ^{13}C depletion of particles. It is likely that our rate experiments, which were carried out with water collected from below the hypoxic layers, underestimated the CH_4-assimilation rates that

produced the $\delta^{13}C$ minimum, partially accounting for the discrepancies in our calculations. It is also important to consider that the incorporation of other biologically available gaseous hydrocarbons, such as propane and ethane (Valentine et al. 2010), may have additionally contributed to ^{13}C depletion of suspended particles.

Interestingly, we measured modest, but easily detectable, rates of N_2-fixation (Fig. 3.8 B) despite the high concentrations of $NO_3^- + NO_2^-$ (10 – 13 μmol L^{-1}, Fig. 3.4 B) at depth. We used the "bubble method" (Montoya et al. 1996) for our rate experiments, meaning that our rate estimates may be conservative, though our own comparisons show no difference between the bubble and pre-equilibration methods (Mohr et al. 2010) for incubations lasting a day or longer (Montoya, unpublished data). Rates of N_2-fixation did not correlate well with other parameters, though only a limited number of experiments were performed. Based on previous work in deep waters near natural seep sites in the Northern Gulf, we had expected to see a strong relationship with CH_4-assimilation rates, as we hypothesize that coupled methanodiazotrophy may be a common response to natural gas injection in these environments (Montoya et al., in prep). Though we did find evidence of diazotrophy in the nitrate- and methane-replete shelf waters around the Hercules rig, the weak relationship between N_2-fixation rates and CH_4-assimilation rates (Fig. 3.8) suggests that these two pathways are at least partially decoupled.

3.5.4 Inter-cruise Comparison

The sampling expedition carried out by the C-IMAGE consortium one month after the blowout extends our timeline for assessing the impact of the blowout and the ecosystem response. Just three weeks after our rapid response cruise, hypoxic layers in the water column were no longer present and methane concentrations had dropped

significantly to near background values (Fig. 3.9). Given our finding that the local residence time of subsurface water during our study was at least several days (Fig. 3.10 B), the low CH_4 concentrations in late August imply that the wellhead was no longer releasing appreciable quantities of CH_4, and that the local ecosystem impact of the release had largely ended.

3.6 Conclusion

The Hercules 265 blowout event released large quantities of methane into the surrounding waters in the Northern Gulf of Mexico. We documented clear biogeochemical evidence for a marine microbial ecosystem response to the blowout and could estimate the time scale of exposure of the local water column to the released hydrocarbons. The impact included a significant drawdown of dissolved oxygen to hypoxic conditions, the incorporation of methane-derived carbon into the food web, and modest promotion of N_2-fixation at depth. Though we could not quantify the duration of the release or the total amount of methane discharged, our estimates of water residence time suggest that the flow of methane was severely reduced or completely halted when the well self-sealed. Within one month of the blowout, the ecosystem had returned to pre-blowout conditions. This study highlights the need for focused rapid response efforts in combination with repeated sampling to resolve the nature and timescale of microbial responses to sudden environmental perturbations associated with oil and gas harvesting.

CHAPTER 4

INITIAL CHARACTERIZATION OF DEEP WATER DIAZOTROPHS AND METHANOTROPHS USING NANOSIMS[†]

Sarah C. Weber[1], Joseph P. Montoya[1], Samantha B. Joye[2], Angela Vogts[3], Maren Voss[3]

[1] School of Biology, Georgia Institute of Technology, Atlanta, GA, 30332, USA

[2] Department of Marine Sciences, University of Georgia, Athens, GA 30609, USA

[3] Department of Biological Oceanography, Leibniz Institute for Baltic Sea Research, Warnemünde, Germany

[†] Manuscript in preparation

4.1 Abstract

Recent field studies have revealed uncovered a novel linkage between the carbon and nitrogen cycles through the stimulation of deepwater nitrogen fixation near anthropogenic and natural (i.e. cold seeps) releases of methane. As a first step in characterizing the organism(s) oxidizing methane and fixing nitrogen in deep waters, we performed NanoSIMS analyses on tracer-incubated samples. We found direct evidence of $^{13}CH_4$ and $^{15}N_2$ incorporation into organic matter, though in distinct, spatially separated structures that appear to be derived from free-living cells or cellular aggregates. Enrichments of ^{15}N were found within aggregates (1 and10 μm in diameter) and were commonly associated with sulfur-rich regions, whereas ^{13}C enrichments occurred only in independently distributed particles (< 0.5 μm) and small aggregates (< 3 μm). Our rate measurements imply nitrogen turnover times of roughly 40 d due to N_2-fixation and carbon turnover times due to CH_4-assimilation of ~227 d. When compared to our bulk measurements, specific rates of N_2-fixation implied that the average diazotrophic contribution to total nitrogen was 1.61 ± 1.17 %. Taken together, these data imply that these metabolic processes are occurring in different cells. Although diazotrophy may not be the primary N acquisition strategy for deepwater seep-associated microbial communities, N_2-fixation is occurring and appears to be stimulated by both natural and anthropogenic injections of CH_4 into the water column.

4.2 Introduction

The Deepwater Horizon oil spill of 2010 was the largest such disaster in history, with the release of an estimated 5 million barrels of oil and over 350,000 tonnes of methane and other gases (Joye et al. 2011). Though large quantities of oil and gas made it to the surface, a large plume of oil and gas at ~1000 m depth moved laterally to the southwest of the wellhead (Camilli et al. 2010; Valentine et al. 2010). During a research cruise one month after the well was sealed, we measured both low $\delta^{13}C$ and low $\delta^{15}N$ in suspended particles within this deep plume (Fernández et al., in review). The low $\delta^{13}C$ signatures are attributable to incorporation of ^{13}C-depleted petro-carbon into particulate organic matter, whereas the low $\delta^{15}N$ signatures (-2 to 0 ‰, Montoya et al. 2007) are typically associated with nitrogen fixation and could not have been influenced by the petro-carbon directly. In addition to ^{15}N depletion in particles within the deep-water plume, we also measured significant rates of N_2-fixation within the plume layer (Montoya et al., in prep), representing a previously undescribed linkage between the C and N cycles deep in the water column.

As a natural analogue to anthropogenic releases of oil/gas, we have studied the influence of cold seeps on local N and C cycling in the water column. Using combined $^{15}N_2$ and $^{13}CH_4$ tracer additions in paired "in plume" and "out of plume" experiments, we have found replicated evidence for the stimulation of N_2-fixation in the water column above active seeps, though we have not yet been able to quantify the assimilation of CH_4 into bulk biomass (Montoya et al., in prep) or to identify the organisms responsible. Our findings suggest that these processes are linked, and we hypothesize that N_2-fixing methanotrophic archaea may be responsible. In this context, N_2-fixation is a secondary

consequence of the injection of oil and gas into the water column, and an important coupling between the marine carbon and nitrogen cycles.

Here we use the new analytical capabilities presented by NanoSIMS technology to explore the spatial distribution of N_2-fixation and CH_4-assimilation in natural microbial populations of the Gulf of Mexico. This approach complements our prior and ongoing efforts to measure the rates of these processes in deep waters of the Gulf of Mexico, and provides a direct test of our hypothesis that methanodiazotrophs, with the metabolic capabilities to both assimilate CH_4 and fix N_2, are responsible for the elevated rates of N_2-fixation that we've observed in subsurface waters affected by natural and anthropogenic injections of CH_4.

4.3 Materials & Methods

Rate experiments were conducted in July 2013 aboard the R/V *Endeavor*. Samples were collected from the water column directly above an active cold seep on Bush Hill (Lease Block GC185, 27.783 ˚N, -91.507 ˚W, Fig. 4.1) and ~200 m outside of the seep bubble plume using a CTD rosette. The shipboard echosounder system (Knudsen 3260) was used to localize the gas plume and guide our sampling by ensuring that we kept the CTD package within the plume during our "in plume" sampling (Fig. 4.2). Water samples were collected at four depths (ranging from 330 – 538 m) at both of the "in plume" and "out of plume" sites. Four 4 L polycarbonate bottles equipped with silicone septum caps were filled from each depth, three of which were used for bulk rate experiments and the fourth for cell-specific rate experiments. Here I will report bulk and cell-specific measurements made from only the deepest "in plume" sample (538 m).

4.3.1 Bulk Assimilation Rates

The three 4 L bottles for bulk rates were amended with 3 mL $^{15}N_2$ (99 at %, Cambridge Isotope) and 0.05 mL $^{13}CH_4$ (98 at %, Sigma-Aldrich) following the protocol of Montoya et al (1996), resulting in substrate enrichments of 5.1 at % ^{15}N in N_2 and 66.7 at % ^{13}C in CH_4. After 48 h of incubation in the dark at *in situ* temperatures, the experiment was terminated by gentle pressure filtration through a 10 µm Nitex prefilter (47 mm diameter) followed by a precombusted 25 mm GF/F filter. Material collected on the 10 µm prefilter was rinsed onto a precombusted 25 mm GF/C filter. Filters were immediately transferred to an oven to dry at 60˚C, and then stored in sealed plastic centrifuge tubes over desiccant.

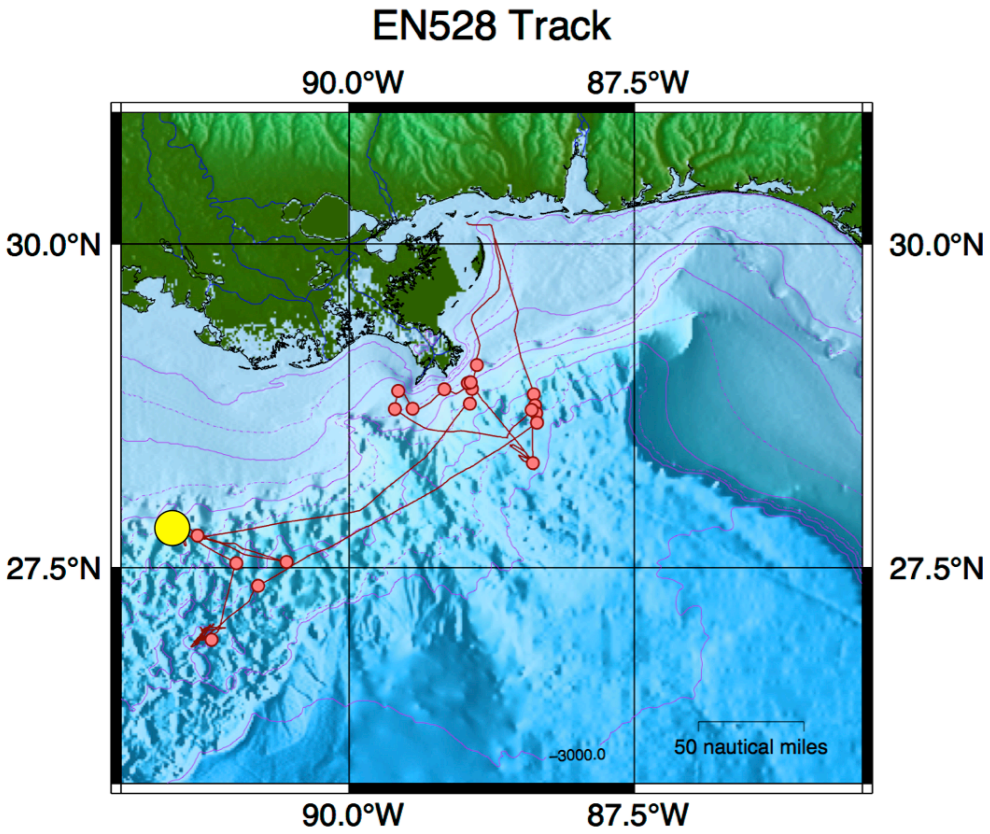

Figure 4.1: Track of cruise EN528 aboard the R/V *Endeavor* off the coast of Louisiana in the Northern Gulf of Mexico. The yellow circle marks the location of the Bush Hill cold seep site (Lease Block GC185) where samples were collected.

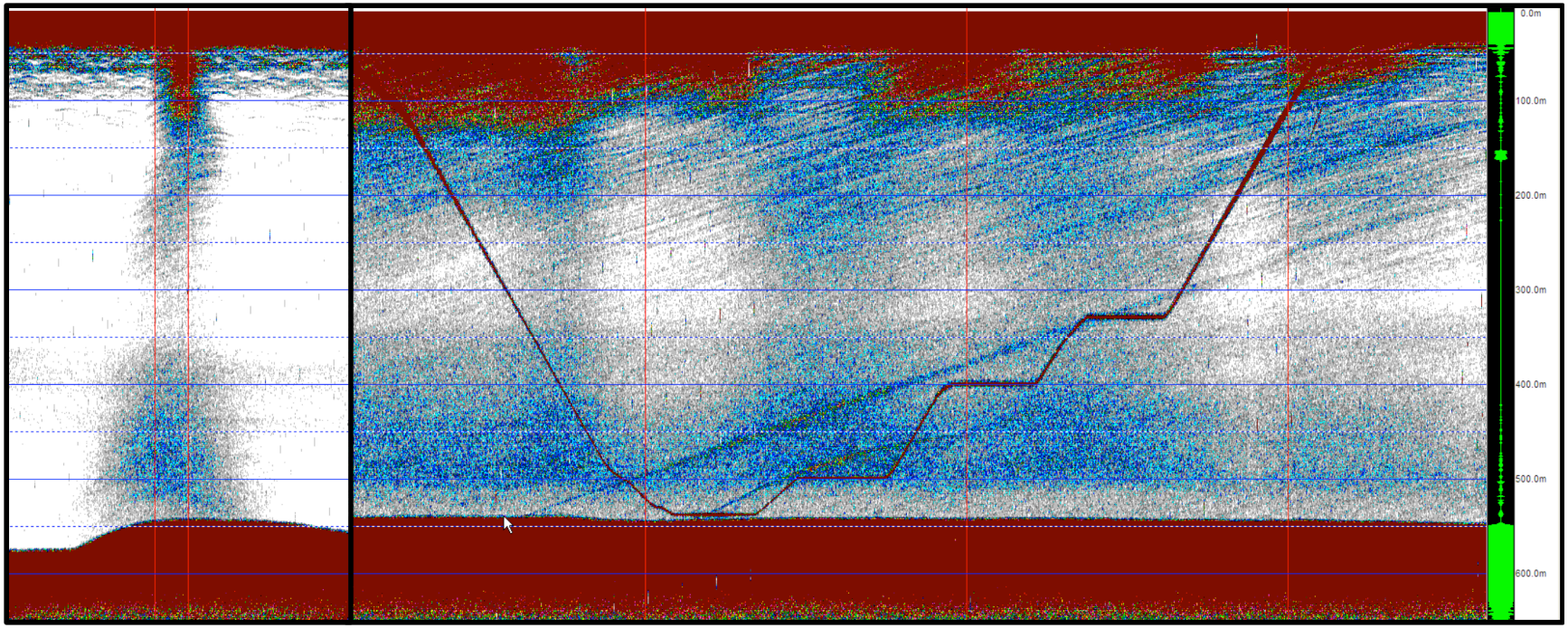

Figure 4.2: (Left) CHIRP echograms of the Bush Hill cold seep (Lease Block GC185). Gas bubbles appear as the lower-density features in blue. The depth of the seafloor (red at bottom of images) is roughly 545 m. **(Right)** Time-lapse of the CHIRP profile over the course of sampling. The CTD (marked by the red line) remained within the bubble plume for the duration of sampling.

Once ashore, samples were encapsulated in tin and analyzed by CF-IRMS using a Micromass Optima interfaced to a Carlo Erba NA2500 elemental analyzer. Each analytical run included a size series of elemental (methionine) and isotopic (peptone) standards, which provided a check on the stability of the instrument and allowed us to remove the contribution of any analytical blank from our isotopic measurements (Montoya 2008). We conservatively estimate that the overall analytical precision of our isotopic measurements is better than ± 0.1‰. We used the mass balance approach of Montoya et al. (1996) to calculate specific rates of the < 10 μm size fraction of N_2-fixation and CH_4-assimilation (rates for the > 10 μm size fraction were undetectable). We used an average $\delta^{13}C$ of -45‰ for water column CH_4 in our rate calculations.

4.3.2 Cell-Specific Assimilation Rates

The remaining 4 L bottle was amended with larger quantities of tracer (10 mL $^{15}N_2$ and 0.2 mL $^{13}CH_4$) to enhance biomass tracer enrichment for cell-specific rate analysis by NanoSIMS. These tracer additions resulted in substrate enrichments of 14.6 at % ^{15}N in N_2 and 88.3 at % ^{13}C in CH_4. Incubation conditions were identical to those used for the bulk rate experiment. This incubation was terminated by gentle vacuum filtration onto a 0.2 μm gold-sputtered polycarbonate filter (25 mm diameter). The sample was then frozen for transport and storage, and prior to analysis in 2015, the filter was dried at 55˚C in a laminar flow hood, taking care to avoid dust contamination.

Analyses were performed at the Institut für Ostseeforschung Warnemünde (Warnemünde, Germany) using a NanoSIMS 50L instrument (Cameca, Gennevilliers, France). Filters were first examined using a compound microscope to identify potential targets for NanoSIMS analysis. We then surveyed large regions (100 x 100 μm) using

the total ion counts (TIC) produced by the primary cesium ion beam to identify areas that contained potential cell aggregates or other intriguing structures. Features of interest were then analyzed further by rastering a small section (10 x 10 to 50 x 50 μm) with the primary cesium ion beam and collecting the generated secondary ions ($^{12}C^-$, $^{13}C^-$, $^{16}O^-$, $^{12}C^{14}N^-$, $^{12}C^{15}N^-$, and $^{32}S^-$) simultaneously in multiple electron multiplier detectors. The Look@NanoSIMS software package (Polerecky et al. 2012) was used to generate ion images and to flag regions of interest (ROIs) based on their elemental and/or isotopic composition. In view of the typical analytical uncertainty in measuring light stable isotope abundances by NanoSIMS (~20 ‰, Hoppe et al. 2013) we conservatively used a threshold of several hundred ‰ as a criterion for active assimilation of isotopically labeled substrate. Using ratios of $^{13}C^-/^{12}C^-$ and $^{12}C^{15}N^-/^{12}C^{14}N^-$, we calculated mass-specific rates (nmol nmol^{-1} h^{-1} or h^{-1}) of N_2-fixation and CH_4-assimilation using the mass balance approach of Montoya et al. (1996). The potential diazotroph contribution to bulk N was calculated by dividing the specific rate of N_2-fixation of a given ROI by the average specific rate of N_2-fixation of our bulk analyses (Table 4.1). This calculation could not be performed for CH_4-assimilation, as ^{13}C enrichment in our bulk samples was undetectable.

4.4 Results

We initially carried out a broad-scale survey of the sample to characterize the distributions of elements and isotopes at relatively low resolution (100 x 100 μm). We identified a variety of organic structures that were enriched in ^{15}N or ^{13}C, reflecting the incorporation of either labeled N_2 or CH_4, respectively, into organic matter. These enriched features ranged in size from < 0.5 to ~1 μm and varied in their physical setting; some features were clearly associated with aggregations of organic matter, while some appeared to be derived from free-living cells. The aggregates ranged in size from 1 to 10 μm in mean diameter and were haphazardly distributed on the sample filter.

Following our initial analysis, we performed a focused, high-resolution reanalysis of ROIs with high isotopic abundance. The destructive nature of NanoSIMS analysis complicates the interpretation of repeated analyses of a feature since each analysis ablates sample material. Only features that have appreciable depth will persist through multiple cycles of analysis.

The higher-resolution analyses revealed that regions of ^{15}N or ^{13}C enrichment include both aggregate-associated and spatially isolated structures (Figs. 4.3, 4.4). In general, ^{15}N-enriched regions were associated with the large, coherent aggregates, though not all aggregates examined included these putative diazotrophs (Fig. 4.5). The most coherent example of ^{15}N assimilation occurred within an aggregate of ~10 μm diameter which included a distinct sulfur-rich area near the region of ^{15}N accumulation (Fig. 4.3 - 24a). The ^{15}N-rich features were < 0.5 μm in diameter and were arrayed around the sulfur-rich feature near the center of the aggregate. The mass-specific rates of N_2-fixation of these ROIs averaged $1.13 \pm 0.64 \times 10^{-3}$ (Table 4.1). We found another

instance of ^{15}N enrichment associated with an isolated sulfur-rich structure ~1 μm in size (Fig. 4.4 - 21a) comprised of two ROIs with relatively high average specific N_2-fixation rates of 1.20 ± 0.66 $x10^{-3}$ (Table 4.1). We additionally found several instances of ^{15}N enrichment in particles on/near larger aggregates (Fig. 4.3). The specific rates of N_2-fixation we calculated for these ROIs ranged from 0.28 to 2.35 $x10^{-3}$ h^{-1} with an overall average of 1.03 ± 0.64 $x10^{-3}$ (Fig. 4.5, Table 4.1). The potential contribution of diazotrophs (^{15}N-enriched ROIs) to bulk organic nitrogen ranged between 0.45 and 4.37 %.

All of the ^{13}C-enriched regions we found were small in size (0.5 – 1 μm) and were either individual particles or part of smaller organic structures (~3 μm). We did not observe any appreciable ^{13}C enrichments associated with large aggregates (~10 μm; Fig. 4.5). In total, specific rates of CH_4-assimilation ranged from 1.25 to 2.64 $x10^{-4}$ h^{-1} with an average of 1.83 ± 0.47 $x10^{-4}$ (Fig 4.5, Table 4.1). Since bulk rates of CH_4-assimilation were undetectable, we could not estimate the potential contributions of putative methanotrophs to bulk C.

	Bulk	Solo	Small agg.	Large agg.	24a (Large agg.)	25c (Small agg.)	Total (Cell-specific)
N_2-fixation rate (h^{-1})	$1.06 \pm 0.24 \times 10^{-5}$	$1.13 \pm 0.87 \times 10^{-3}$	$1.20 \pm 0.66 \times 10^{-3}$	$0.99 \pm 0.67 \times 10^{-3}$	$1.13 \pm 0.64 \times 10^{-3}$	$1.20 \pm 0.66 \times 10^{-3}$	$1.03 \pm 0.64 \times 10^{-3}$
CH_4-assim. rate (h^{-1})	N.D.	$1.96 \pm 0.47 \times 10^{-4}$	$1.63 \pm 0.44 \times 10^{-4}$	N.D.	N.D.	N.D.	$1.83 \pm 0.47 \times 10^{-4}$

Table 4.1: Biomass-specific rates of N_2-fixation and CH_4-assimilation for various size classes and analyses. Bulk rates were measured with EA-IRMS, whereas rates in the other categories are cell-specific and were analyzed with NanoSIMS. Values represent averages ± SD. Note that CH_4-assimilation rates are an order of magnitude lower than rates of N_2-fixation. N.D. = not detected.

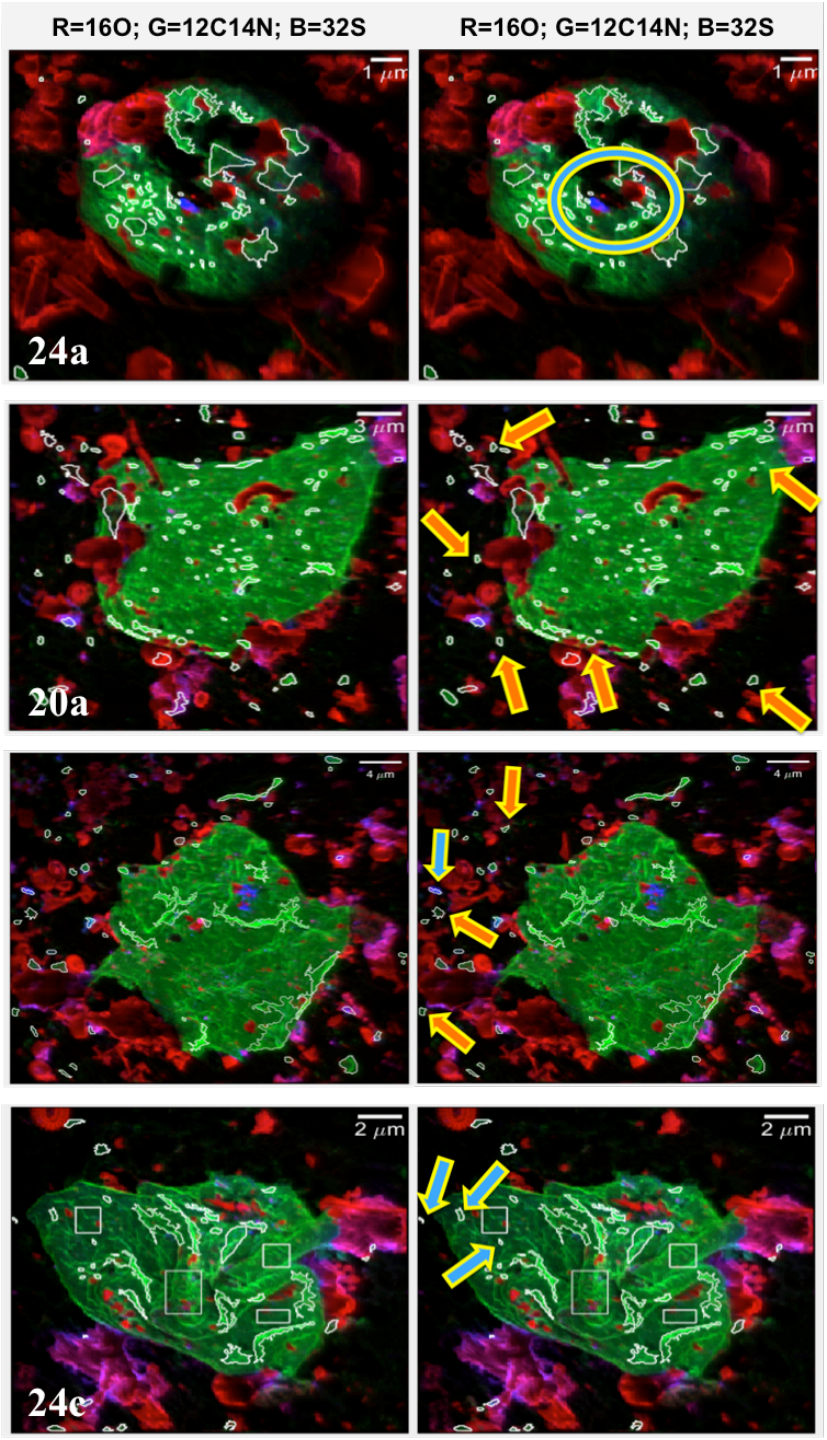

Figure 4.3: NanoSIMS ion images of large aggregates from tracer incubated samples. Images are paired such that the right image is a labeled version of the left. Blue arrows and ovals denote regions of significant ^{15}N enrichment, whereas orange arrows mark significant ^{13}C enrichment. Note that the scale bars differ between paired analyses.

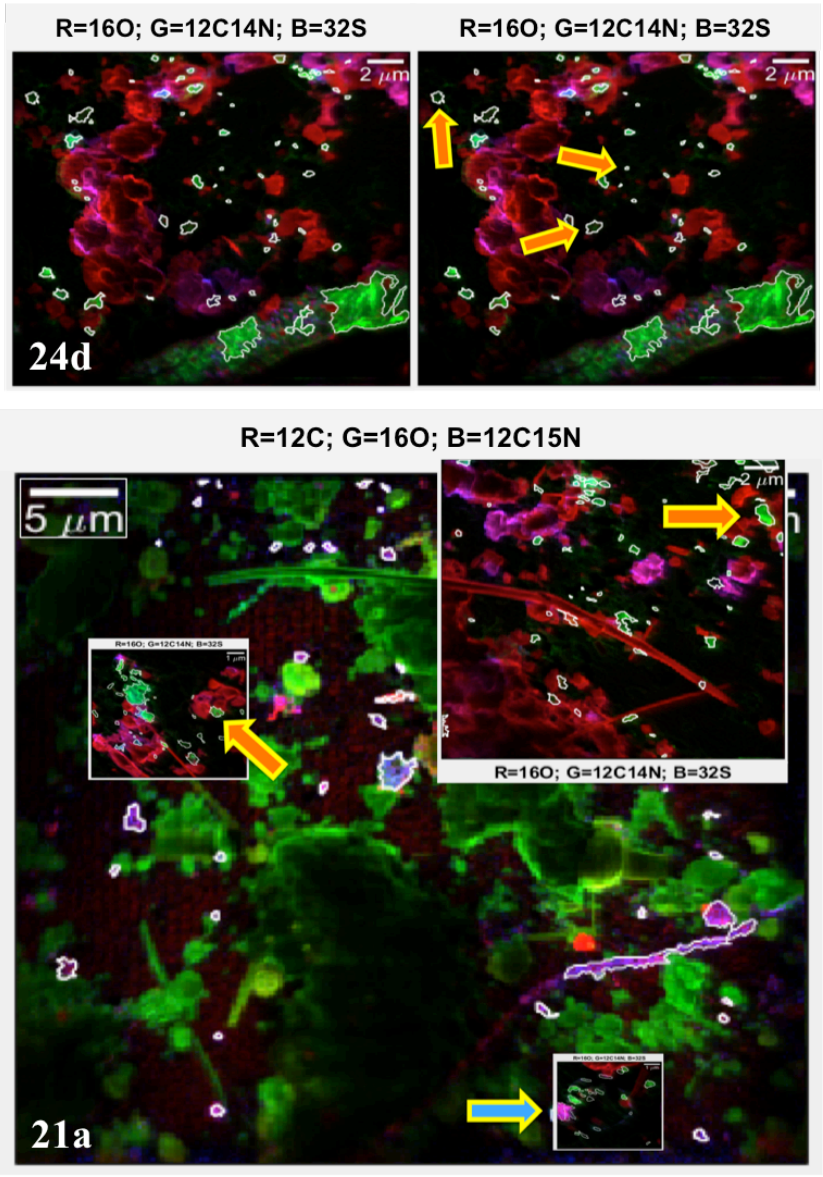

Figure 4.4: NanoSIMS ion images of ^{15}N (blue arrow) and ^{13}C (orange arrows) enrichments in individual particles and small aggregates. The upper two images are paired (unlabeled and labeled), and the three insets in 21a in bottom image are detailed analyses aligned with a larger, low-resolution scan. The image color scheme in the low-resolution image of 21a (R=^{12}C; G=^{16}O; B=$^{12}C^{15}N$) differs from that of the high-resolution insets and that of 24d (R=^{16}O; G=$^{12}C^{14}N$; B=^{32}S).

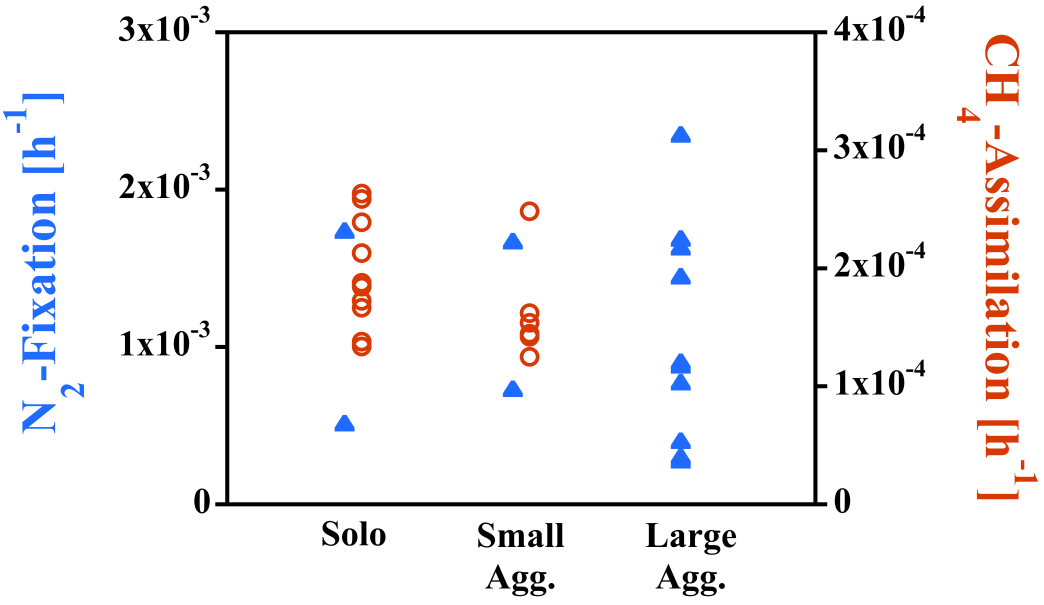

Figure 4.5: Mass-specific rates of N_2-fixation and CH_4-assimilation by region type: individual particles (solo), regions associated with small aggregates < 3 µm in diameter (small agg.), and those associated with large aggregates ~10 µm in diameter (large agg.).

4.5 Discussion

Using NanoSIMS analyses, we have taken the first steps towards physically characterizing the organisms involved in methane oxidation and N_2-fixation near natural seep sites. Our initial measurements have revealed organic-rich regions that are enriched in either ^{13}C or ^{15}N following incubation in the presence of $^{13}CH_4$ and $^{15}N_2$, confirming that labeled CH_4 and N_2 were assimilated into organic matter. Interestingly, these two metabolic processes do not appear to occur within the same cells or aggregates and are instead spatially segregated. Enrichments of ^{15}N were often associated with larger aggregates (~10 μm) and particularly with structures with high sulfur content. This suggests that the active diazotrophs typically reside in or on relatively large detrital particles where they can potentially utilize suboxic microenvironments to fix nitrogen. The association with sulfur enrichments suggests that N_2-fixation may be metabolically linked to sulfur metabolism.

The specific rates of N_2-fixation we measured with NanoSIMS are orders of magnitude higher than the bulk rates measured in parallel experiments, but are surprisingly low if N_2-fixation comprises the primary source of nitrogen supporting growth of the labeled cells. The mean nitrogen turnover time implied by our specific rates is 40 d, which suggests that other sources of N may make an important contribution to the overall N demand of these organisms.

The NanoSIMS approach provides a focused tool for assessing microbial physiology at the cellular level, effectively removing the burden of non-diazotrophic N from our rate estimates. A comparison of the bulk and NanoSIMS derived rates provides insight into the fraction of nitrogen within the bulk sample that was actively fixing N_2.

The estimated contribution of diazotrophs to total nitrogen depends on the specific N_2-fixation rate, and varies from 0.45 and 4.37 %, with an overall mean of 1.61 %. Thus, our data imply that diazotrophs comprised a relatively minor portion of the nitrogen pool in deep waters, though their activity was easily detectable in bulk samples.

In contrast, we found ^{13}C enrichment primarily in small (< 0.5 μm), individual particles, which may be free-living cells or cell fragments, and were less commonly part of small aggregates (1 to 3 μm). The small quantities of ^{13}C incorporated into organic matter relative to the large unlabeled pool of C in our samples explains why we were unable to detect $^{13}CH_4$ assimilation with conventional EA-IRMS methods, which in turn prevents us from estimating the fraction of the bulk C pool associated with methanotrophs. The specific rates of CH_4 assimilation we measured imply a carbon turnover time of 227 d, which is surprisingly long compared to typical microbial growth rates. If CH_4 is the primary carbon and energy source for these organisms, then the metabolic partitioning of assimilated CH_4 between biomass and catabolic products may be a critical factor limiting our ability to measure CH_4 assimilation experimentally.

We began this study with an initial hypothesis that N_2-fixation and CH_4 assimilation were linked and that diazotrophic methanotrophs were the organisms responsible for deepwater N_2-fixation in the presence of natural and anthropogenic injections of CH_4 into the water column. Instead, the distinct spatial segregation of ^{15}N and ^{13}C labeling in our samples suggests that different organisms are responsible for diazotrophy and methanotrophy, though the two processes must still be linked metabolically in some way given the clear association we've found between CH_4 injections and N_2-fixation in deep waters of the Gulf of Mexico. As we move forward

with characterizing these organisms, we will explore alternative methods of sample preservation (e.g. paraformaldehyde), link our incubations to other microbiological identification techniques (e.g. FISH), and expand our analysis to organisms collected at other cold seep sites in the Gulf of Mexico. We will also investigate the factors that may limit CH_4 assimilation into biomass, including respiratory processes that may produce ^{13}C-labeled CO_2.

CONCLUSIONS

Large rivers were conventionally thought to be net sources of carbon dioxide, but more recent studies have reshaped this idea. Through the delivery of phosphate and silicate rich waters to the nitrogen-limited surface waters of the WTNA, the Amazon River plume fertilizes the region in a way that promotes diazotrophy (N_2-fixation). Of particular interest are Diatom-Diazotroph Assemblages (DDAs) such as *Hemiaulus hackii – Richelia intracellularis*; we used various biogeochemical approaches to show that this DDA contributes diazotrophic nitrogen to the local food web and enhances the biological export of carbon in the plume periphery. Though the distributions of these DDAs were primarily shaped by nutrient concentrations, our data show that the instantaneous physical/chemical conditions of the plume alone are not predictive of blooms. Time, or specifically the duration of exposure to preferential habitat, also plays a critical role. In this text, we have restricted our analysis to the spring high-flow period, but an inter-seasonal comparison of phytoplankton biogeography would help elucidate the full impact of DDA blooms on both regional and global carbon drawdown.

To our knowledge, our study on the Hercules 265 natural gas blowout was the first to document the immediate environmental impact of an anthropogenic release of oil/gas on a marine pelagic ecosystem. Using a suite of physical and biogeochemical measurements, we found strong evidence for significant biological drawdown of oxygen and methane near the wellhead within just one week of the blowout, and a return to pre-blowout conditions within one month. The unpredictability of these blowout events combined with the complicated logistics of mobilizing scientific resources on short notice

makes it exceedingly difficult to study the early stages of a blowout. Without the happenstance of the disaster occurring near the end of a major, planned expedition to the area, we would not have been able to mount a field study so quickly, or to characterize the timescale of response of the native microbial community. This study highlights the need for rapid response efforts in the wake of such anthropogenic perturbations, as they will only become more common in our continued harvest of offshore oil and gas.

With our research focusing on oil/gas spills and cold seeps in the Gulf of Mexico, we have uncovered a surprising relationship between methane releases and the stimulation of diazotrophy in deep waters. Our efforts to describe this process began with measurements of natural abundances of stable isotopes and accompanying rate experiments using stable isotope tracer techniques. We then turned to nano-scale isotope imaging using a NanoSIMS instrument to characterize the structure and physical relationships among organisms utilizing diazotrophy and methane-assimilation. We found that these metabolisms are carried out in separate organisms and have identified a number of general physical and chemical motifs associated with these processes. As we continue our investigations into this intriguing relationship between methane releases and diazotrophy, we will explore additional ways to identify and characterize these organisms. When paired with microbiological techniques such as FISH, NanoSIMS can bridge the gap between biogeochemistry and microbiology, opening up the "black box" of biogeochemical rate measurements to identify the organisms involved in critical processes.

REFERENCES

Barker, J. F. and P. Fritz (1981). "Carbon isotope fractionation during microbial methane oxidation." Nature **293**(5830): 289-291.

Berner, R. A. and J. L. Rao (1994). "Phosphorus in Sediments of the Amazon River and Estuary - Implications for the Global Flux of Phosphorus to the Sea." Geochimica Et Cosmochimica Acta **58**(10): 2333-2339.

Bloch, S. and R. M. Key (1981). "Modes of Formation of Anomalously High Radioactivity in Oil-Field Brines." Aapg Bulletin-American Association of Petroleum Geologists **65**(1): 154-159.

Brzezinski, M. A. (1985). "The Si-C-N Ratio of Marine Diatoms - Interspecific Variability and the Effect of Some Environmental Variables." Journal of Phycology **21**(3): 347-357.

Bugna, G. C., J. P. Chanton, et al. (1996). "The importance of groundwater discharge to the methane budgets of nearshore and continental shelf waters of the northeastern Gulf of Mexico." Geochimica Et Cosmochimica Acta **60**(23): 4735-4746.

Camilli, R., C. M. Reddy, et al. (2010). "Tracking Hydrocarbon Plume Transport and Biodegradation at Deepwater Horizon." Science **330**(6001): 201-204.

Capone, D. G. (2005). "Nitrogen fixation by Trichodesmium spp.: An important source of new nitrogen to the tropical and subtropical North Atlantic Ocean." Global Biogeochemical Cycles **19**.

Capone, D. G., J. P. Zehr, et al. (1997). "Trichodesmium, a globally significant marine cyanobacterium." Science **276**(5316): 1221-1229.

Carpenter, E. J., J. P. Montoya, et al. (1999). "Extensive bloom of a N2-fixing diatom/cyanobacterial association in the tropical Atlantic Ocean." Marine Ecology Progress Series **185**: 273-283.

Carpenter, E. J., A. Subramaniam, et al. (2004). "Biomass and primary productivity of the cyanobacterium Trichodesmium spp. in the tropical N Atlantic ocean." Deep-Sea Research Part I-Oceanographic Research Papers **51**(2): 173-203.

Cherrier, J., J. Sarkodee-Adoo, et al. (2013). "Fossil Carbon in Particulate Organic Matter in the Gulf of Mexico following the Deepwater Horizon Event." Environmental Science & Technology Letters **1**(1): 108-112.

Chong, L. S., W. M. Berelson, et al. (2014). "Carbon and biogenic silica export influenced by the Amazon River Plume: Patterns of remineralization in deep-sea sediments." Deep-Sea Research Part I-Oceanographic Research Papers **85**: 124-137.

Codispoti, L. A. (1989). Phosphorus vs Nitrogen Limitation of New and Export Production.

Codispoti, L. A., J. A. Brandes, et al. (2001). "The oceanic fixed nitrogen and nitrous oxide budgets: Moving targets as we enter the anthropocene?" Scientia Marina **65**: 85-105.

Coles, V. J., M. T. Brooks, et al. (2013). "The pathways and properties of the Amazon River Plume in the tropical North Atlantic Ocean." Journal of Geophysical Research-Oceans **118**(12): 6894-6913.

Cooley, S. R. and P. L. Yager (2006). "Physical and biological contributions to the western tropical North Atlantic Ocean carbon sink formed by the Amazon River plume." Journal of Geophysical Research-Oceans **111**(C8).

Demaster, D. J. and R. H. Pope (1996). "Nutrient dynamics in Amazon shelf waters: Results from AMASSEDS." Continental Shelf Research **16**(3): 263-289.

Dickson, A. G., C. L. Sabine, et al. (2007). "Guide to best practives for ocean CO2 measurements." PICES Special Publication **3**: 191.

Dugdale, R. C. and J. J. Goering (1967). "Uptake of New and Regenerated Forms of Nitrogen in Primary Productivity." Limnology and Oceanography **12**(2): 196-&.

Eppley, R. and B. Peterson (1979). "Particulate Organic-Matter Flux and Planktonic New Production In the Deep Ocean." Nature **282**: 667-680.

Ffield, A. (2007). "Amazon and Orinoco River plumes and NBC rings: Bystanders or participants in hurricane events?" Journal of Climate **20**(2): 316-333.

Foltz, G. R. and M. J. McPhaden (2009). "Impact of Barrier Layer Thickness on SST in the Central Tropical North Atlantic." Journal of Climate **22**(2): 285-299.

Foster, R. A., A. Subramaniam, et al. (2007). "Influence of the Amazon River plume on distributions of free-living and symbiotic cyanobacteria in the western tropical north Atlantic Ocean." Limnology and Oceanography **52**(2): 517-532.

Foster, R. A., A. Subramaniam, et al. (2009). "Distribution and activity of diazotrophs in the Eastern Equatorial Atlantic." Environmental microbiology **11**(4): 741-750.

Fox, L. E., S. L. Sager, et al. (1986). "The chemical control of soluble phosphorus in the Amazon estuary." Geochimica Et Cosmochimica Acta **50**(5): 783-794.

Fratantoni, D. M. and D. A. Glickson (2002). "North Brazil current ring generation and evolution observed with SeaWiFS." Journal of Physical Oceanography **32**(3): 1058-1074.

Fry, B. and E. B. Sherr (1984). "Delta-C-13 measurements of carbon flow in marine and fresh-water ecosystems." Contributions in Marine Science **27**(SEP): 13-47.

Goericke, R., J. P. Montoya, et al. (1994). Physiology of isotope fractionation in algae and cyanobacteria. Stable Isotopes in Ecology and Environmental Science. K. Lajtha and B. Michener. Oxford, Blackwell Scientific Publications**:** 187-221.

Goes, J. I., H. D. R. Gomes, et al. (2014). "Influence of the Amazon River discharge on the biogeography of phytoplankton communities in the western tropical north Atlantic." Progress in Oceanography **120**: 29-40.

Gruber, N. and J. L. Sarmiento (1997). "Global patterns of marine nitrogen fixation and denitrification." Global Biogeochemical Cycles **11**(2): 235-266.

Gruber, N. and J. L. Sarmiento (2002). "Large-Scale Biogeochemical-Physical Interactions In Elemental Cycles." The sea **12**.

Hawser, S. P., J. M. Oneil, et al. (1992). "Toxicity of Blooms of the Cyanobacterium Trichodesmium to Zooplankton." Journal of Applied Phycology **4**(1): 79-86.

Hoefs, J. (1987). Stable Isotope Geochemistry. Berlin, Springer.

Hoppe, P., S. Cohen, et al. (2013). "NanoSIMS: Technical Aspects and Applications in Cosmochemistry and Biological Geochemistry." Geostandards and Geoanalytical Research **37**(2): 111-154.

Jahnke, L. L., R. E. Summons, et al. (1999). "Carbon isotopic fractionation in lipids from methanotrophic bacteria II: the effects of physiology and environmental parameters on the biosynthesis and isotopic signatures of biomarkers." Geochimica et Cosmochimica Acta **63**(1): 79-93.

Johnson, K. M., A. G. Dickson, et al. (1998). "Coulometric total carbon dioxide analysis for marine studies: assessment of the quality of total inorganic carbon measurements made during the US Indian Ocean CO2 Survey 1994-1996." Marine Chemistry **63**(1-2): 21-37.

Johnson, K. M., K. D. Wills, et al. (1993). "Coulometric Total Carbon-Dioxide Analysis for Marine Studies - Maximizing the Performance of an Automated Gas Extraction System and Coulometric Detector." Marine Chemistry **44**(2-4): 167-187.

Joye, S. B., I. R. MacDonald, et al. (2011). "Magnitude and oxidation potential of hydrocarbon gases released from the BP oil well blowout." Nature Geoscience **4**(3): 160-164.

Kendall, C., S. R. Silva, et al. (2001). "Carbon and nitrogen isotopic compositions of particulate organic matter in four large river systems across the United States." Hydrological Processes **15**(7): 1301-1346.

Kortzinger, A. (2003). "A significant CO2 sink in the tropical Atlantic Ocean associated with the Amazon River plume." Geophysical Research Letters **30**(24).

Kraemer, T. F. and D. F. Reid (1984). "The occurrence and behavior of radium in saline formation water of the U.S. Gulf Coast region." Chemical Geology **46**(2): 153-174.

Krest, J. M., W. S. Moore, et al. (1999). "Ra-226 and Ra-228 in the mixing zones of the Mississippi and Atchafalaya Rivers: indicators of groundwater input." Marine Chemistry **64**(3): 129-152.

Laws, E. A., B. N. Popp, et al. (1995). "Dependence of phytoplankton carbon isotopic composition on growth rate and $[CO_2]_{aq}$: Theoretical considerations and experimental results." Geochimica et Cosmochimica Acta **59**: 1131-1138.

Lentz, S. J. and R. Limeburner (1995). "The Amazon River Plume During AMASSEDS - Spatial Characteristics and Salinity Variability." Journal of Geophysical Research-Oceans **100**(C2): 2355-2375.

Lohrenz, S. E., G. L. Fahnenstiel, et al. (1997). "Variations in primary production of northern Gulf of Mexico continental shelf waters linked to nutrient inputs from the Mississippi River." Marine Ecology-Progress Series **155**: 45-54.

Loick-Wilde, N., S. C. Weber, et al. (2015). "Nitrogen sources and net growth efficiency of zooplankton in three Amazon River plume food webs " Limnology and Oceanography **In press**.

Longhurst, A. (1993). "Seasonal cooling and blooming in tropical oceans." Deep Sea Research Part I: Oceanographic Research **40**: 2145-2165.

Magen, C., L. L. Lapham, et al. (2014). "A simple headspace equilibration method for measuring dissolved methane." Limnology and Oceanography-Methods **12**: 637-650.

Mathieu, G. G., P. E. Biscaye, et al. (1988). "Systems for Measurement of Rn-222 at Low-Levels in Natural-Waters." Health Physics **55**(6): 989-992.

Mikaloff Fletcher, S. E., N. Gruber, et al. (2007). "Inverse estimates of the oceanic sources and sinks of natural CO2 and the implied oceanic carbon transport." Global Biogeochemical Cycles **21**: 1-19.

Modin, O., K. Fukushi, et al. (2007). "Denitrification with methane as external carbon source." Water Research **41**(12): 2726-2738.

Mohr, W., T. Grosskopf, et al. (2010). "Methodological Underestimation of Oceanic Nitrogen Fixation Rates." Plos One **5**(9): 7.

Montoya, J. P. (2008). Nitrogen stable isotopes in marine environments. Nitrogen in the Marine Environment. D. G. Capone, E. J. Carpenter, M. R. Mulholland and D. A. Bronk, Academic press**:** 1277-1302.

Montoya, J. P. (2008). "Nitrogen Stable Isotopes in Marine Environments." Nitrogen in the Marine Environment, 2nd Edition: 1277-1302.

Montoya, J. P., E. J. Carpenter, et al. (2002). "Nitrogen fixation and nitrogen isotope abundances in zooplankton of the oligotrophic North Atlantic." Limnology and Oceanography **47**(6): 1617-1628.

Montoya, J. P., C. M. Holl, et al. (2004). "High rates of N-2 fixation by unicellular diazotrophs in the oligotrophic Pacific Ocean." Nature **430**(7003): 1027-1031.

Montoya, J. P. and M. Voss (2006). Nitrogen cycling in suboxic waters: Isotopic signatures of nitrogen transformations in the Arabian Sea Oxygen Minimum Zone. Past and Present Water Column Anoxia. L. Neretin. Dordrecht, the Netherlands, Springer. **64:** 259-281.

Montoya, J. P., M. Voss, et al. (2007). "Spatial variation in N2-fixation rate and diazotroph activity in the Tropical Atlantic." North: 369-376.

Montoya, J. P., M. Voss, et al. (1996). "A simple, high-precision, high-sensitivity tracer assay for N-2 fixation." Applied and Environmental Microbiology **62**(3): 986-993.

Moore, W. S. (2000). "Determining coastal mixing rates using radium isotopes." Continental Shelf Research **20**(15): 1993-2007.

Moore, W. S. and R. Arnold (1996). "Measurement of Ra-223 and Ra-224 in coastal waters using a delayed coincidence counter." Journal of Geophysical Research-Oceans **101**(C1): 1321-1329.

Moore, W. S. and D. F. Reid (1973). "Extraction of Radium from Natural-Waters Using Manganese-Impregnated Acrylic Fibers." Journal of Geophysical Research **78**(36): 8880-8886.

Muller-Karger, F. E., C. R. McClain, et al. (1988). "The Dispersal of the Amazon's Water." Nature **333**(6168): 56-59.

Muller-Karger, F. E., P. L. Richardson, et al. (1995). "On the offshore dispersal of the Amazon ' s Plume in the North Atlantic : Comments on the paper by A . Longhurst , " Seasonal cooling and blooming in tropical oceans "." Deep Sea Research Part I: Oceanographic Research Papers **42**: 2127-2137.

Naqvi, S. W. A., H. W. Bange, et al. (2010). "Marine hypoxia/anoxia as a source of CH4 and N2O." Biogeosciences **7**(7): 2159-2190.

NOAA. (2013). "NOAA-supported Scientists Find Large Gulf Dead Zone, but Smaller than Predicted." Retrieved Aug 20, 2014, from http://www.noaanews.noaa.gov/stories2013/2013029_deadzone.html.

Peterson, R. N., W. C. Burnett, et al. (2009). "Comparison of measurement methods for radium-226 on manganese-fiber." Limnology and Oceanography-Methods **7**: 196-205.

Peterson, R. N., W. C. Burnett, et al. (2008). "Radon and radium isotope assessment of submarine groundwater discharge in the Yellow River delta, China." Journal of Geophysical Research-Oceans **113**(C9): 14.

Peterson, R. N., R. F. Viso, et al. (2013). "On the utility of radium isotopes as tracers of hydrocarbon discharge." Marine Chemistry **156**: 98-107.

Polerecky, L., B. Adam, et al. (2012). "Look@NanoSIMS - a tool for the analysis of nanoSIMS data in environmental microbiology." Environmental Microbiology **14**(4): 1009-1023.

Rabalais, N. N., R. J. Diaz, et al. (2010). "Dynamics and distribution of natural and human-caused hypoxia." Biogeosciences **7**(2): 585-619.

Rabalais, N. N., R. E. Turner, et al. (2007). "Hypoxia in the northern Gulf of Mexico: Does the science support the plan to reduce, mitigate, and control hypoxia?" Estuaries and Coasts **30**(5): 753-772.

Rau, G. H., U. Riebesell, et al. (1996). "A model of photosynthetic ^{13}C fractionation by marine phytoplankton based on diffusive molecular CO_2 uptake." Marine Ecology Progress Series **133**: 275-285.

Scranton, M. I. and P. G. Brewer (1977). "Occurence of Methane in Near-Surface Waters of Western Subtropical North-Atlantic." Deep-Sea Research **24**(2): 127-138.

Sigman, D. M., M. A. Altabet, et al. (2000). "The delta N-15 of nitrate in the Southern Ocean: Nitrogen cycling and circulation in the ocean interior." Journal of Geophysical Research-Oceans **105**(C8): 19599-19614.

Smith, S. V. (1984). "Phosphorus Versus Nitrogen Limitation in the Marine Environment." Limnology and Oceanography **29**(6): 1149-1160.

Smith, W. O. and D. J. Demaster (1996). "Phytoplankton biomass and productivity in the Amazon River plume: Correlation with seasonal river discharge." Continental Shelf Research **16**(3): 291-319.

Strickland, J. D. H. and T. H. Parson (1972). "A practical handbook of seawater analysis." Ottowa: Fisheries Research Board of Canada: 310.

Stukel, M. R., V. J. Coles, et al. (2014). "Top-down, bottom-up and physical controls on diatom-diazotroph assemblage growth in the Amazon River plume." Biogeosciences **11**(12): 3259-3278.

Subramaniam, A., P. L. Yager, et al. (2008). "Amazon River enhances diazotrophy and carbon sequestration in the tropical North Atlantic Ocean." Proceedings of the National Academy of Sciences of the United States of America **105**(30): 10460-10465.

Sweeney, C., D. A. Hansell, et al. (2000). "Biogeochemical regimes, net community production and carbon export in the Ross Sea, Antarctica." Deep-Sea Research Part Ii-Topical Studies in Oceanography **47**(15-16): 3369-3394.

Takahashi, T., S. C. Sutherland, et al. (2002). "Global sea – air CO2 flux based on climatological surface ocean pCO2 , and seasonal biological and temperature effects." Deep Sea Research Part II: Topical Studies in Oceanography **49**: 1601-1622.

Valentine, D. L., J. D. Kessler, et al. (2010). "Propane Respiration Jump-Starts Microbial Response to a Deep Oil Spill." Science **330**(6001): 208-211.

Villareal, T. A. (1989). "Division Cycles in the Nitrogen-Fixing Rhizosolenia (Bacillariophyceae) Richelia (Nostocaceae) Symbiosis." British Phycological Journal **24**(4): 357-365.

Villareal, T. A. (1990). "Laboratory Culture and Preliminary Characterization of the Nitrogen-Fixing Rhizosolenia-Richelia Symbiosis." Marine Ecology-Pubblicazioni Della Stazione Zoologica Di Napoli I **11**(2): 117-132.

Vorosmarty, C., B. Fekete, et al. (2000). "Global system of rivers: Its role in organizing continental land mass and defining land-to-ocean linkages." Global Biogeochemical **14**: 599-621.

Voss, M., D. Bombar, et al. (2006). "Riverine influence on nitrogen fixation in the upwelling region off Vietnam, South China Sea." Geophysical Research Letters **33**(7).

Voss, M., J. Dippner, et al. (2001). "Nitrogen isotope patterns in the oxygen deficient waters of the Eastern Tropical North Pacific (ETNP)." Deep-Sea Research **48**: 1905-1921.

Yeung, L. Y., W. M. Berelson, et al. (2012). "Impact of diatom-diazotroph associations on carbon export in the Amazon River plume." Geophysical Research Letters **39**: 1-6.

Zehr, J. P. and B. B. Ward (2002). "Nitrogen cycling in the ocean: New perspectives on processes and paradigms." Applied and Environmental Microbiology **68**(3): 1015-1024.